KOPIO TN053

Beam aspect ratio and FastMC acceptance

David E. Jaffe, BNL

March 27, 2003

Abstract

I compared the signal-to-background (S/B) *vs* signal (S) rates for four different beam aspect ratios ranging from 68×7.3 mrad^2 to 130×3.8 mrad^2. For the Konaka PreRadiator (PR) model, there is no significant difference between the different aspect ratios at the 10% level. For the Zeller PR, the 68×7.3 mrad^2 and 81×6.1 mrad^2 configurations have a $20 \pm 5\%$ and $18 \pm 5\%$ reduction in S/B for the same signal yield compared to the 100×5 mrad^2, respectively. The loss appears to be due to degradation of resolution as the vertical beam divergence increases.

Contents

1 Introduction

The TDR [1] is based on a beam aspect ratio defined by (horizontal $\times$ vertical) collimation of 100×5 mrad^2. From mechanical considerations of the beam pipe, a narrower and taller beam is desirable. The suppression of neutron halo is less effective with a narrower and taller beam and resolution on reconstructed quantities is expected to be worse due to the less restrictive constraint on the vertical position of the K_L^0.

Jaap Doornbos did a comparison of the neutron halo for four different beam aspect ratios in TechNote TN049 [2]. I used Figure 19 from TN049, reproduced here as Figure 1, to determine the x and y values at Z=1400 cm where the neutron halo was

10^{-4} of the beam. These values are plotted and shown in Figure 3. As a check, I compared the 0.01% contours given by these values with the lower, right hand plot of Figure 20 from TN049 (0.02% contour), reproduced here as Figure 2. An earlier FastMC study [3] found acceptable background levels for neutron halo/beam of 10^{-4}.

Jaap's note assumes an extended target and beam to define beam aspect ratios. The FastMC assumes a point source for K^0_L, so I redefined the beam aspect ratios.

I based my redefinition on $\Theta_x \times \Theta_y = 50 \times 2.5$ as the aspect ratio for the beam used in the TDR and I assume that this aspect ratio corresponds to Jaap's aspect #1. To obtain Θ_y for the FastMC for aspect #2, I scaled by the Jaap's ratios of Θ_y for aspects #1 and #2. Then I set Θ_x such that the solid angle, $\Delta\Omega$, is 500 μSR.

I use the clearances derived from Jaap's results at Z = 1400 cm and the FastMC beam aspect ratios, Table 1, to define the inner aperture at **Z = 1350 cm**, the front of the PR.

2 Definitions

Here are definitions of terms and variables used in this note.

- $\Theta_{x(y)}$ = beam half angle in x(y) when describing the size of the beam envelope; note, however, in Section 4, that $|\Theta_{X(Y)}|$ is the magnitude of the production angle in X(Y) of the K^0_L,
- BeamX(Y) = beam half size in x(y) at a given Z,
- HaloX(Y) = X(Y) position where Halo/Beam= 10^{-4},
- **clearance** = ClearX(Y) = HaloX(Y) −BeamX(Y) is the distance between the edge of the K^0_L beam envelope and the envelope where Halo/Beam= 10^{-4} in X(Y),
- FidSiz = fiducial size of PR front face assuming outer limits $150 \times 150\text{cm}^2$.
- $\delta \equiv \sqrt{\delta_x^2 + \delta_y^2}$ where $\delta_x(\delta_y)$ is the difference in x(y) between measured e^- and e^+ positions at last plane used for measurement,
- $P^*(\pi^0)$ is the magnitude of the momentum of the π^0 in the K^0_L CMS,
- $E(\gamma)$ is the photon energy in the lab,
- $E^*(\gamma)$ is the photon energy in the K^0_L CMS, and
- $A_{X(Y)}$ is the the production angle in X(Y) of the photon.

The definitions also appear elsewhere in the note.

	Jaap		FastMC		
	milliradians				μSR
Aspect#	Θ_x	Θ_y	Θ_x	Θ_y	$\Delta\Omega$
1	51	2.6	50	2.5	500
2	42	3.2	40.625	3.077	500.01
3	35	3.8	34.2105	3.654	500.02
4	66	2.0	65	1.923	499.98

Table 1: Comparison of beam aspect ratios used in Jaap's note [2] and in the FastMC for this note. Θ_x and Θ_y are beam half-angles. The total solid angle subtended by the beam is $\Delta\Omega$.

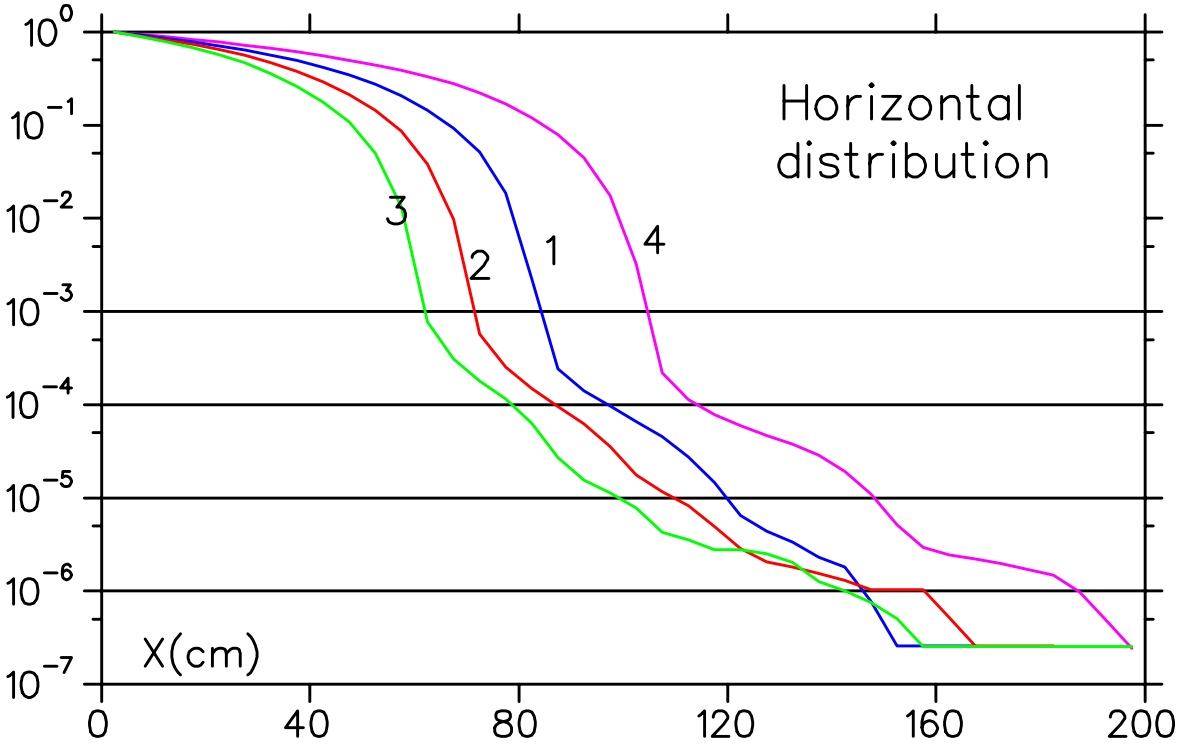

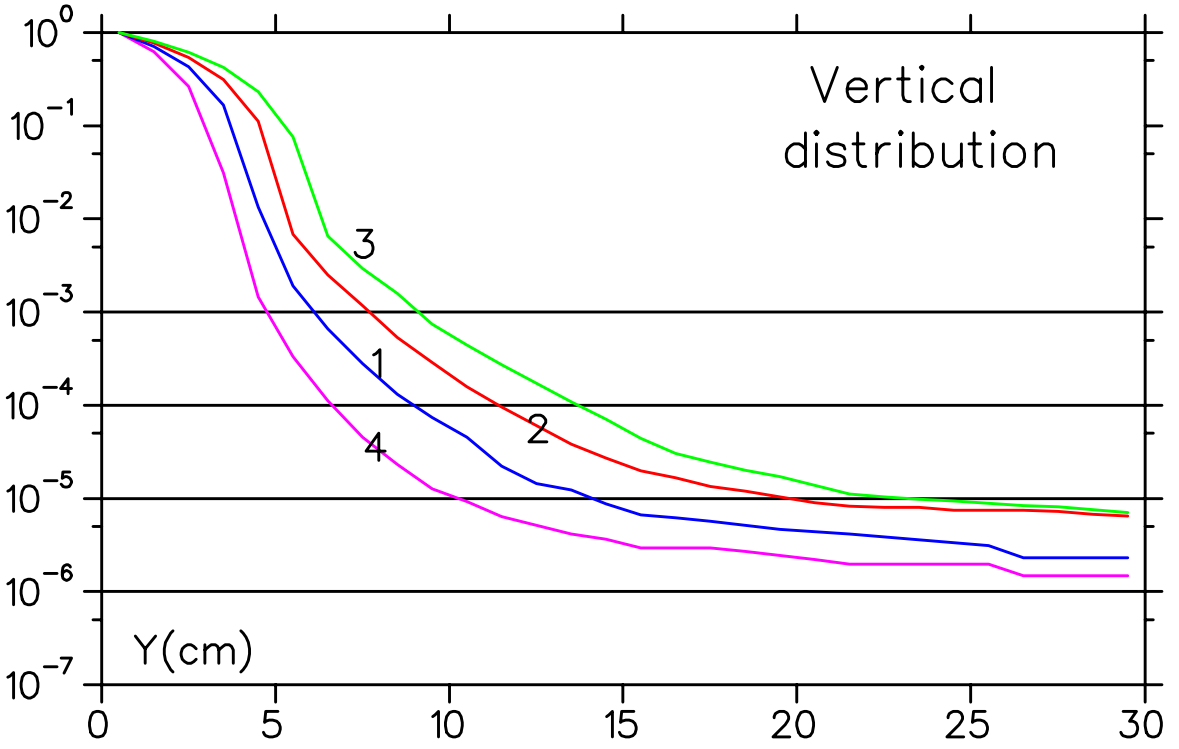

Figure 1: This is Figure 19 of TN049: ‘ ‘Fraction of beam outside the areas, indicated on the horizontal axis.”

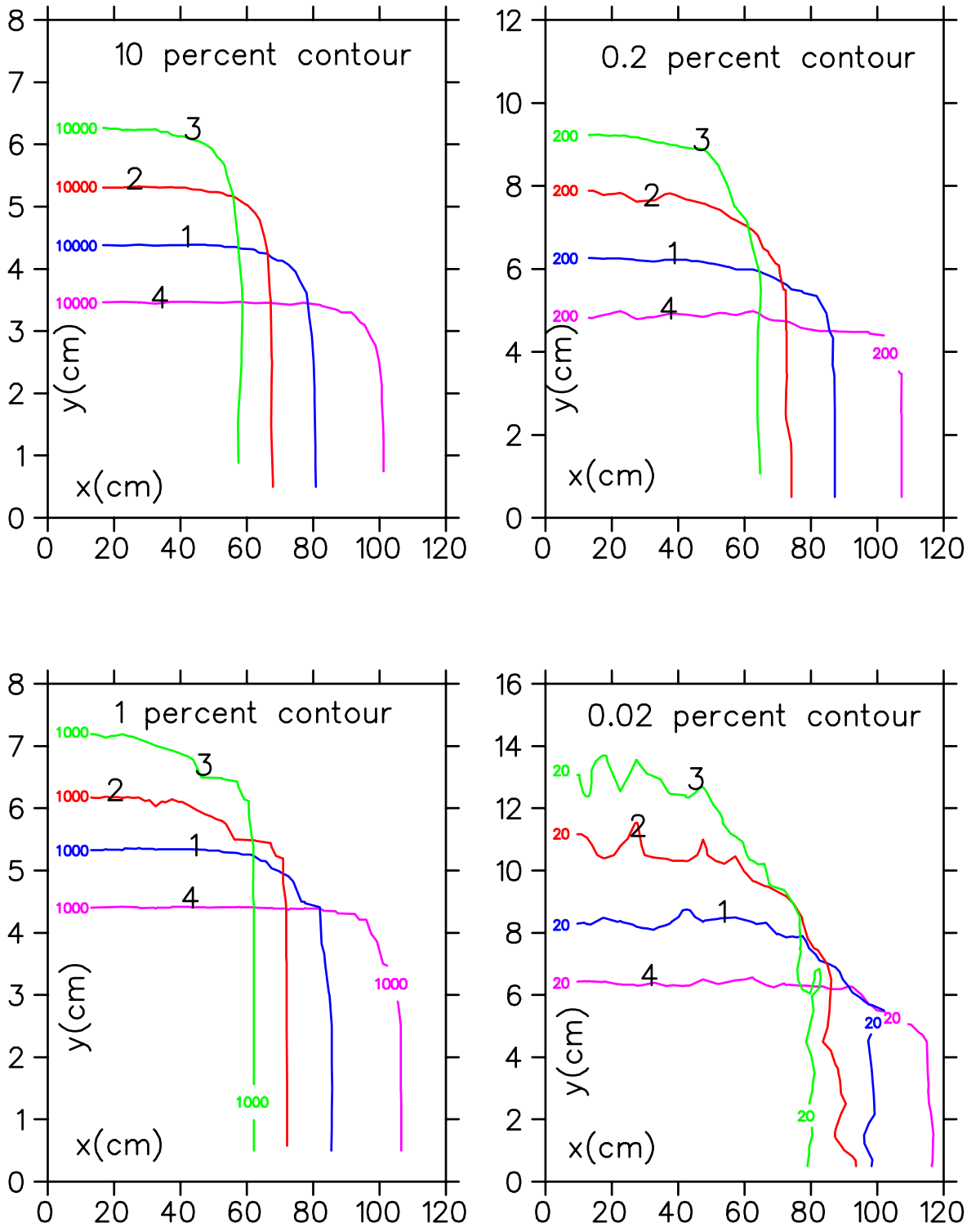

Figure 2: This is Figure 20 of TN049: "Contour plots at 14 m."

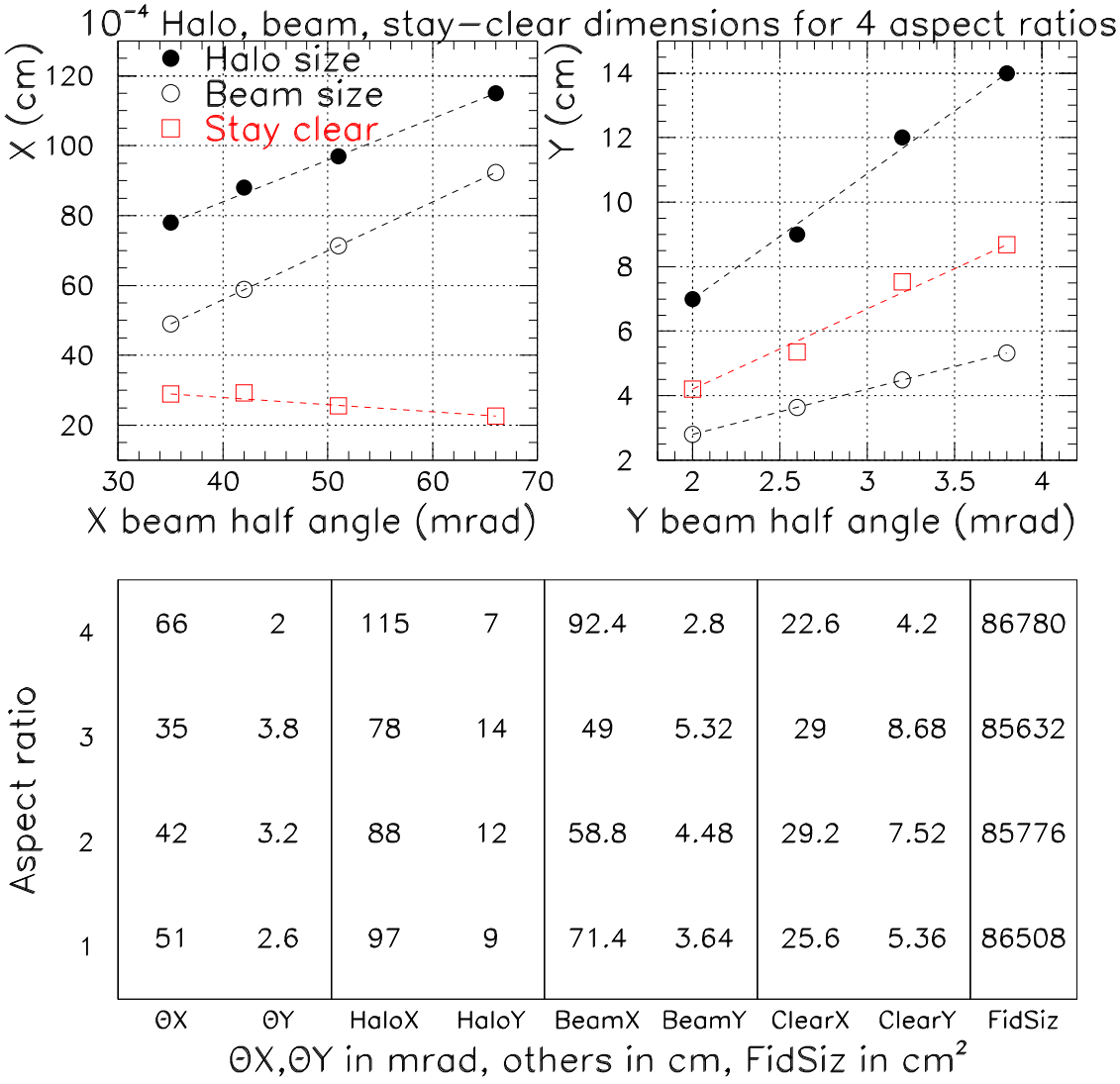

Aspect ratio	ΘX	ΘY	HaloX	HaloY	BeamX	BeamY	ClearX	ClearY	FidSiz
4	66	2	115	7	92.4	2.8	22.6	4.2	86780
3	35	3.8	78	14	49	5.32	29	8.68	85632
2	42	3.2	88	12	58.8	4.48	29.2	7.52	85776
1	51	2.6	97	9	71.4	3.64	25.6	5.36	86508

Figure 3: Definitions of quantities in the figure: Θ_x, Θ_y = beam half angle, BeamX,BeamY = beam half size, HaloX,HaloY = X,Y position where Halo/Beam= 10^{-4}, ClearX,ClearY = clearance = Halo −Beam, FidSiz = fiducial size of PR front face assuming outer limits $150 \times 150\text{cm}^2$. Note that the fiducial size differs by less than 1.5% between the four aspect ratios.

3 Scope of this study

For the rest of the note, I will refer to aspect ratios in terms of the *full* opening angles instead of the half opening angles.

- I assume a 2.4 second spill with a 2.3 second interspill and a total running time of 12000 hours. The primary proton beam is assumed to be 70 TP/spill. The total number of K_L^0 exiting the spoiler is 1.271×10^{16}. The $K_L^0 \to \pi^0\nu\bar{\nu}$ branching fraction is taken to be 3×10^{-11}. The K_L^0 momentum spectrum is taken from Kapinos [4] for 45°. I assume no production angle dependence of the K_L^0 flux across the horizontal aperture.

- This note reports the acceptance for **both** photons converting in PR. The case of one photon converting in the calorimeter and the other in the PR is not treated.

- The cuts used for comparison were optimized for the 100×5 mrad^2 geometry with clearance ∞ cm $\times$ 14.975 cm. The infinite horizontal clearance was the result of a coding error. The vertical clearance was based on aperture defined by the "half angle of the vertical hole" (= "ycal") of 10 milliradians, the Z position of the CAL (= "zcal") of 1480 cm and an additional 5 cm, thus, Aperture(cm) = $.010 \times 1480 + 5$. Akira Konaka provided an explanation of the origin of the "half angle of the vertical hole":

  " The length of the calorimeter is defined as zcal and the half width of the hole in the calorimeter at the exit of the calorimeter divided by zcal is defined as yang. It looks like I added an extra 5cm to define the effective hole. "

  For this study, 100×5 mrad^2 has clearance 25.6 cm $\times$ 5.36 cm.

- There are seven different sets of cuts used to trace a S/B *vs* signal curve. Six of the seven sets were developed with the Konaka PR model. The remaining set of cuts was developed with the Zeller PR model.

- Only backgrounds from major K_L^0 decay modes are considered: $3\pi^0$, $2\pi^0$, $\pi^+\pi^-\pi^0$ and $\pi e\nu\gamma$. Non-K_L^0 backgrounds and backgrounds from other K_L^0 decays were ignored.

- Photons that pass through the beam hole aperture and traverse the PR are included.

- The input to the fitting procedure is the energy, time, angles and positions of the two photon candidates as detected in the PR/CAL. Two fits are performed. The first constrains the two photons to come from a common space point and time. The second imposes an additional requirement of the π^0 mass on the photon pair. In both fits, the vertical angle of the beam is used as a constraint. Explicitly, the constraint is $Y = 0 \pm \sigma$ where $\sigma = \Theta_Y \times Z_{\rm mid}/\sqrt{12}$, where Θ_Y is the full vertical angle of the beam and $Z_{\rm mid}$ is the middle of the decay volume (1150 cm). Except for the two photon mass, $M(\gamma\gamma)$, all quantities used in further analysis are the result of the second fit.

- Both Konaka and Zeller PR simulations of the PR were tried.

The Konaka PR model [5] uses an energy-dependent double gaussian to simulate the PR angular resolution. It contains no angular-dependence to the angular resolution.

The Zeller PR model [6] is best described by comments in the code: `A program to reconstruct the response of analog strip pre-radiator for E926. The basic geometry is 2 nested hexagonal tubes with readout between, separated by Pb radiator of thickness TPb (cm). ...Takes average of two analog hits at each plane. Randomize which comes first, x or y. This version has mult scat at each tube.`

For signal events, core resolution on the reconstructed two photon mass $M(\gamma\gamma)$ is significantly worse for Zeller PR and there are larger tails that can be removed with a cut on δ where $\delta \equiv \sqrt{\delta_x^2 + \delta_y^2}$ where $\delta_x(\delta_y)$ is the difference in x(y) between measured e^- and e^+ positions at last plane used for measurement. The dependence of δ on the photon energy is shown in Figure 4. There is no equivalent quantity available from the Konaka PR model. The effect of an energy-dependent cut on δ on $M(\gamma\gamma)$ is shown in Figure 5 after the application of the basic cuts. The **basic cuts** are

1. SKIM CUTS: defined below.
2. FitOK: no singular matrix encountered in the fit,
3. EK: $638 < E(K) < 1486$ MeV where $E(K)$ is the reconstructed candidate K_L^0 energy,
4. ZK: $1025 < Z(K) < 1300$ cm where $Z(K)$ is the Z position of the reconstructed candidate K_L^0,
5. dif: $\delta < max(1., 4. - 0.005 * E_\gamma(MeV))$ cm, where δ is defined above and $E_\gamma(MeV)$ is the fitted photon energy.

The definition of the SKIM CUTS:

- Generated Photon at 10 radiation lengths into PR/CAL $|X| < 300.00, |Y| < 300.00$ cm
- For the reconstructed K_L^0 candidate:
  - $0.00 < E(K) < 1486.00$ MeV and
  - $0.00 < Z(K) < 2000.00$ cm
- For the reconstructed π^0 candidate:
  - $0.00 < E^*(\pi) < 240.00$ MeV
  - $100.00 < M(\gamma\gamma) < 170.00$ MeV/c^2
  - $E^*(\pi) - |E^*(\gamma 1) - E^*(\gamma 2)| > 0.0$ MeV

The SKIM CUTS have been applied for all results presented in this note. I use the relatively loose SKIM CUTS to reduce the size of the FastMC data that I have to store on disk. The **basic cuts** were applied for resolution and bias studies in the next section.

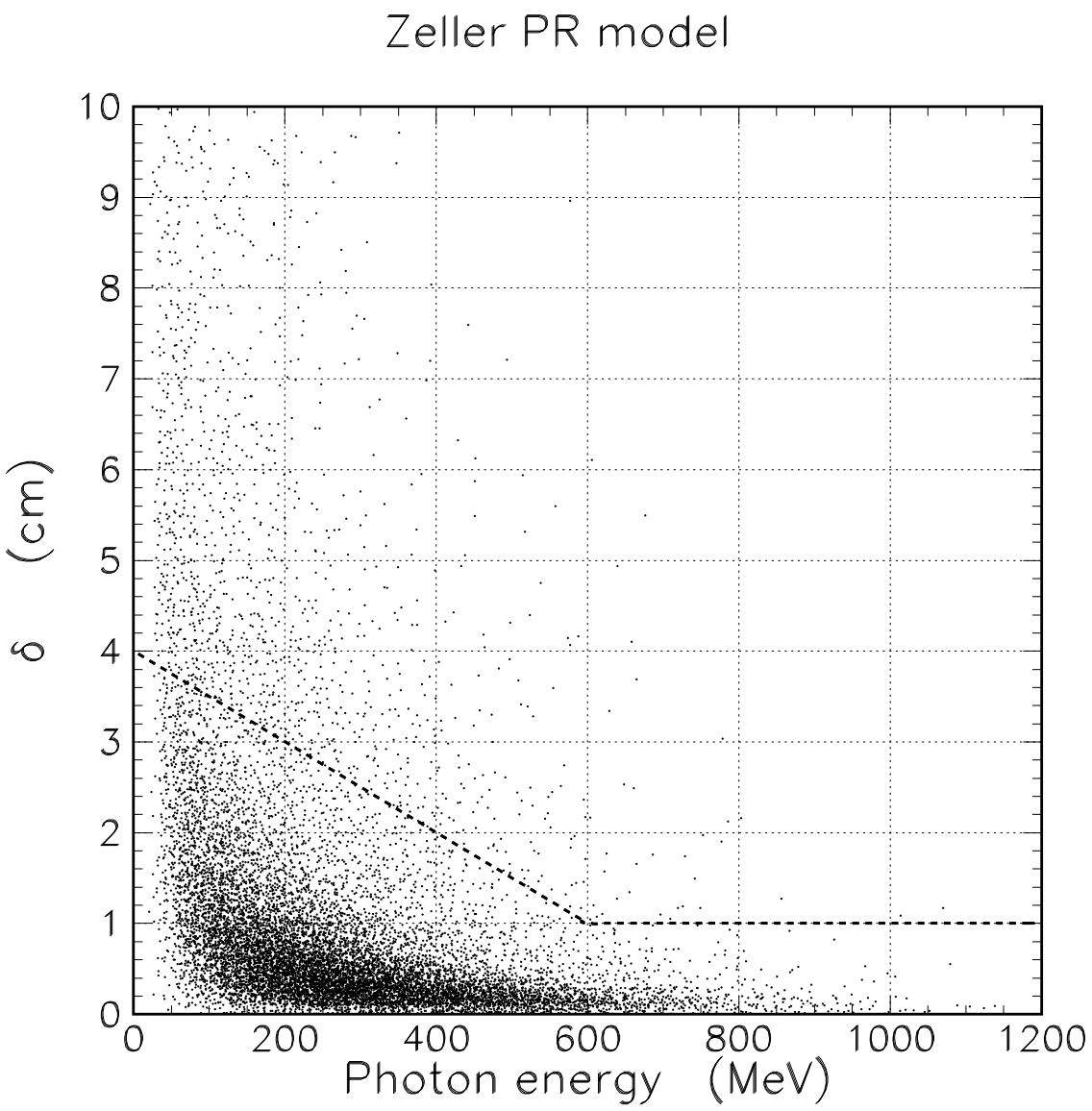

Figure 4: The dependence of $\delta \equiv \sqrt{\delta_x^2 + \delta_y^2}$ on the photon energy for the Zeller PR model after the application of these **basic cuts**: SKIM CUTS, FitOK, EK and ZK. The dashed line shows the cut applied to remove tails. See text for details.

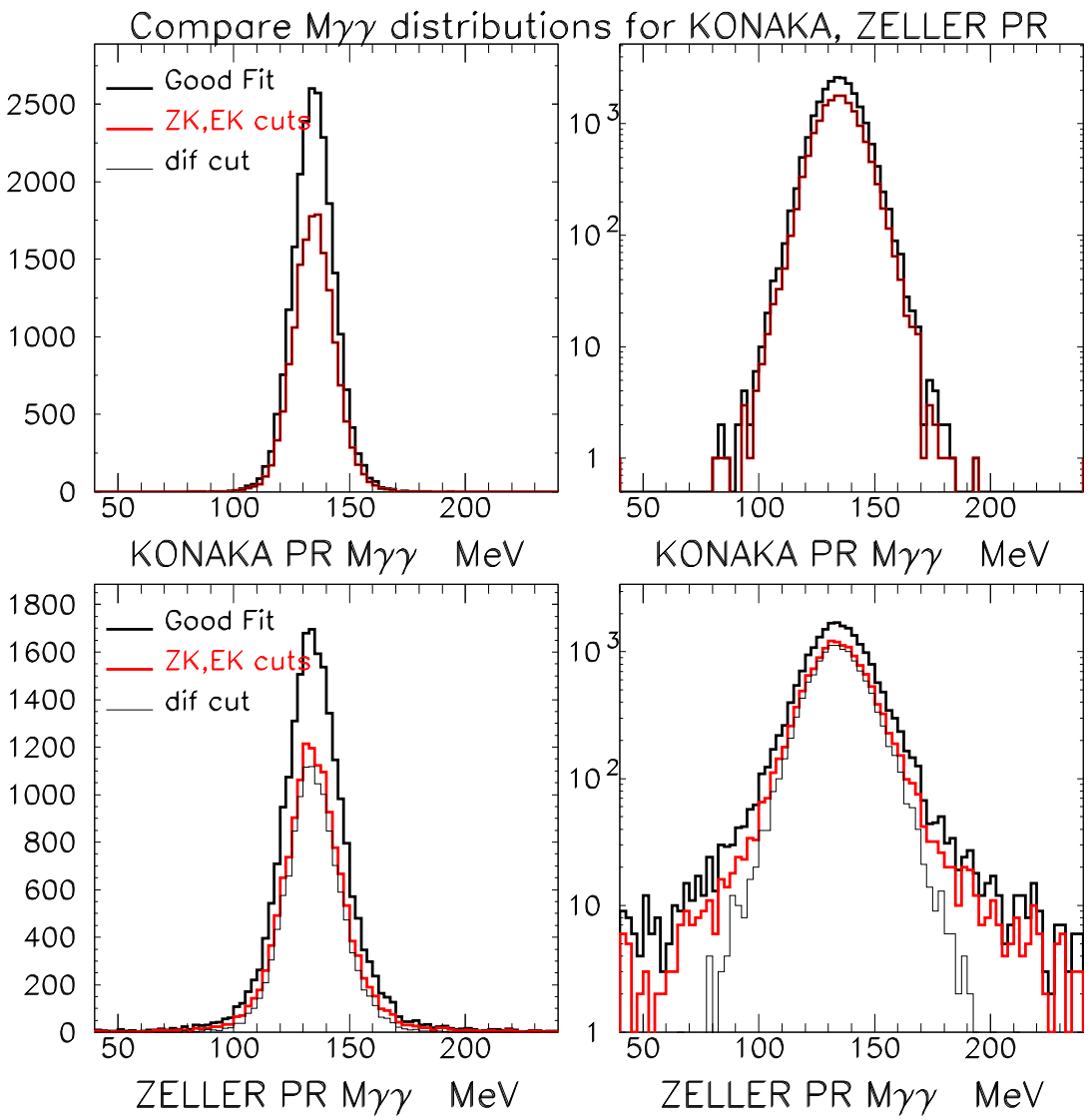

Figure 5: Comparison of $M(\gamma\gamma)$ distributions for the Konaka and Zeller PR models after successive application of basic cuts.

4 Comparison of resolution and bias

I did extensive comparison of the core resolution and the bias of reconstructed and fitted quantities determined by the FastMC. The core resolution is defined as the σ of a gaussian fit to a distribution where the fit is restricted to $\pm 2\sigma$ about the fitted mean (multiple iterations are done for each gaussian fit to obtain a stable value of σ and the mean). The bias is simply the fitted mean of the distribution of the difference of the measured and generated value of a quantity.

The **basic cuts** were applied for the resolution and bias studies.

Figures 6, 7, 8, 9 and 10 show the core resolution on $M(\gamma\gamma)$, $P^*(\pi^0)$, $Z(K)$, $E(\gamma)$ and $E^*(\gamma)$, respectively, as a function of $Z(K)$, $|\Theta_X|$, $|\Theta_Y|$, $E(\gamma)$, $E^*(\gamma)$, $|A_X|$ or $|A_Y|$. $P^*(\pi^0)$ is the magnitude of the momentum of the π^0 in the K^0_L CMS, $|\Theta_{X(Y)}|$ is the magnitude of the production angle in X(Y) of the K^0_L, $E(\gamma)$ is the photon energy in the lab, $E^*(\gamma)$ is the photon energy in the K^0_L CMS, and $|A_{X(Y)}|$ is the magnitude of the production angle in X(Y) of the photon. Figures 11, 12, 13, 14 and 15 show the bias on $M(\gamma\gamma)$, $P^*(\pi^0)$, $Z(K)$, $E(\gamma)$ and $E^*(\gamma)$, respectively.

Figure 6 shows that the $M(\gamma\gamma)$ resolution is significantly worse for the Zeller PR model and that there is a stronger dependence of the resolution on $Z(K)$ than the Konaka PR model. In addition, there is a clear degradation of $M(\gamma\gamma)$ resolution as the K^0_L vertical production angle increases for both models, although the effect is more evident for the Zeller PR model. (This is contrary to previous statements I made that were based on lower statistics.) The overall signal efficiency with the Zeller PR model is $\sim 75\%$ of the signal efficiency with the Konaka PR model mainly due to the the poorer $M(\gamma\gamma)$ resolution.

Figure 7 shows that $P^*(\pi^0)$ resolution degrades with increasing $Z(K)$ in the same manner as $M(\gamma\gamma)$. In addition, the $P^*(\pi^0)$ resolution for the 68×7.3 mrad^2 configuration is about 0.5 MeV/c worse compared to 100×5 mrad^2 for all values of $Z(K)$. The degradation of $P^*(\pi^0)$ resolution as a function of Θ_Y is evident for both models.

Figure 8 shows that the $Z(K)$ resolution improves from ~ 10.5 cm to $\sim 3.5cm$ from the upstream to the downstream end of the fiducial volume for the Zeller PR model, independent of the beam aspect ratio. The $Z(K)$ resolution for Konaka PR model is about 1 cm worse than that of the Zeller PR model.

The lab photon energy resolution improves with $Z(K)$ as shown in Figure 9 independent of the beam aspect ratio. The improvement is relative greater with the Konaka PR model.

Figure 10 shows a stronger dependence of the $E^*(\gamma)$ resolution on $Z(K)$ with the Zeller PR model than the Konaka PR model. There is also a clear degradation in $E^*(\gamma)$ resolution as the K^0_L vertical production angle increases for both models.

The bias on $M(\gamma\gamma)$ in Figure 11 is ~ 0.5 MeV with both PR models and independent of $Z(K)$ and the K^0_L production angle.

There is a slight dependence of the $P^*(\pi^0)$ bias on $Z(K)$ as shown in Figure 12. More importantly, the bias with the Zeller PR model is ~ 0.5 MeV/c greater than with the Konaka PR model. Thus cuts on $P^*(\pi^0)$ designed with the Konaka PR model may be less effective when applied to the the Zeller PR model. Lower and upper limits are set on $P^*(\pi^0)$ to exclude $K^0_L \to 3\pi$ and $K^0_L \to \pi^0\pi^0$, respectively, so a different bias will allow differing amounts of these backgrounds.

There is a relatively strong bias on $Z(K)$ for decays in the most upstream part of

the fiducial volume as shown in Figure 13 and the bias with the Konaka PR model is ~ 1 cm greater than the Zeller PR model independent of $Z(K)$.

The bias on the lab photon energy decreases(increases) with $Z(K)(E(\gamma))$ as shown in Figure 14 independent of beam aspect ratio. There is a strong dependence on $E^*(\gamma)$ of the bias in $E^*(\gamma)$ as shown in Figure 15.

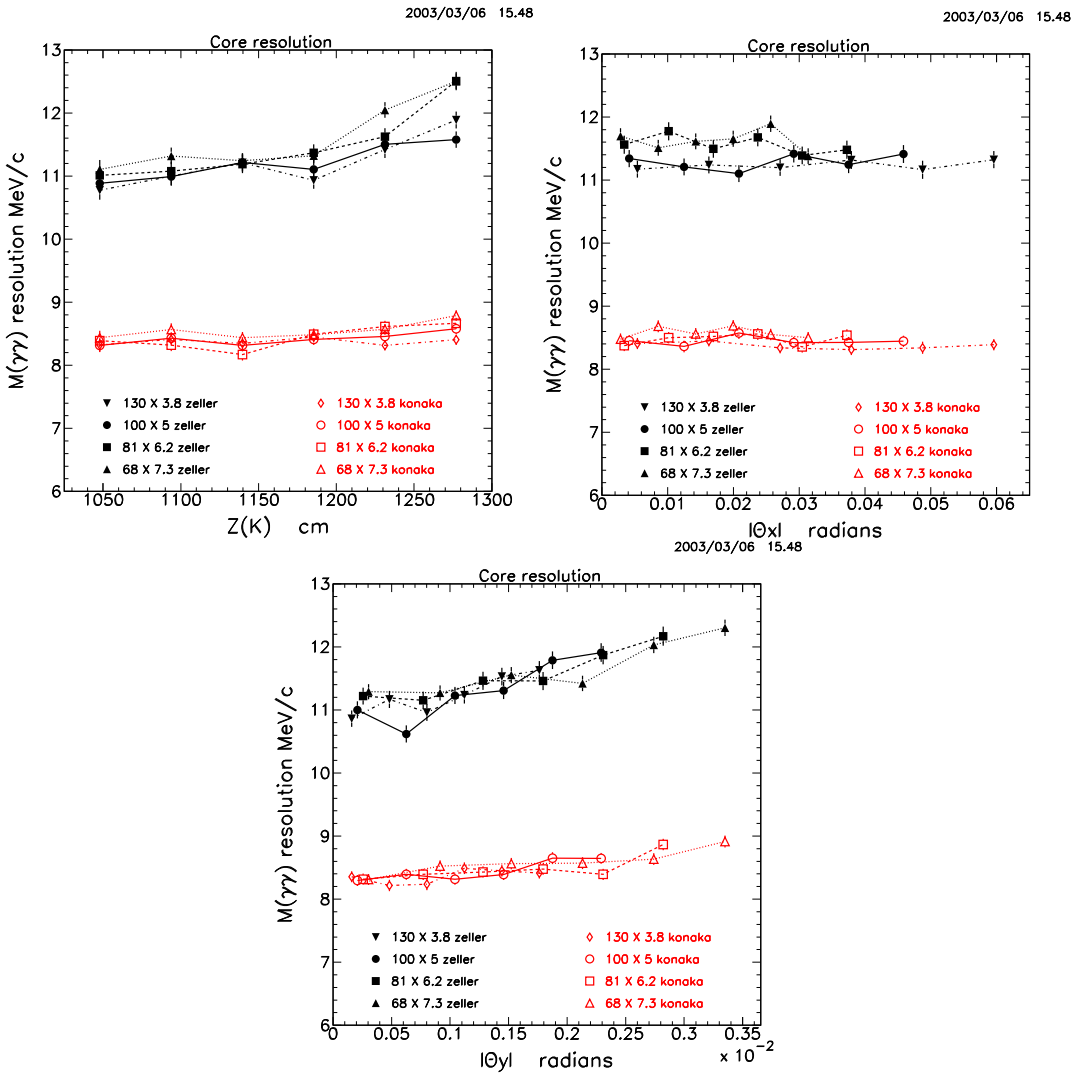

Figure 6: $M(\gamma\gamma)$ core resolution as a function of $Z(K)$, $|\Theta_X|$ and $|\Theta_Y|$ for the Konaka and Zeller PR models for the four different beam aspect ratios after application of basic cuts.

For reference, Figure 16 shows the distributions of $Z(K)$, $E(\gamma)$, $E^*(\gamma)$, $|\Theta_X|$, $|\Theta_Y|$, $|A_X|$ and $|A_Y|$ with the Zeller PR model and the 100×5 mrad^2 aspect ratio after the application of the **basic cuts**. The distributions for the other aspect ratios and with the Konaka PR model are very similar.

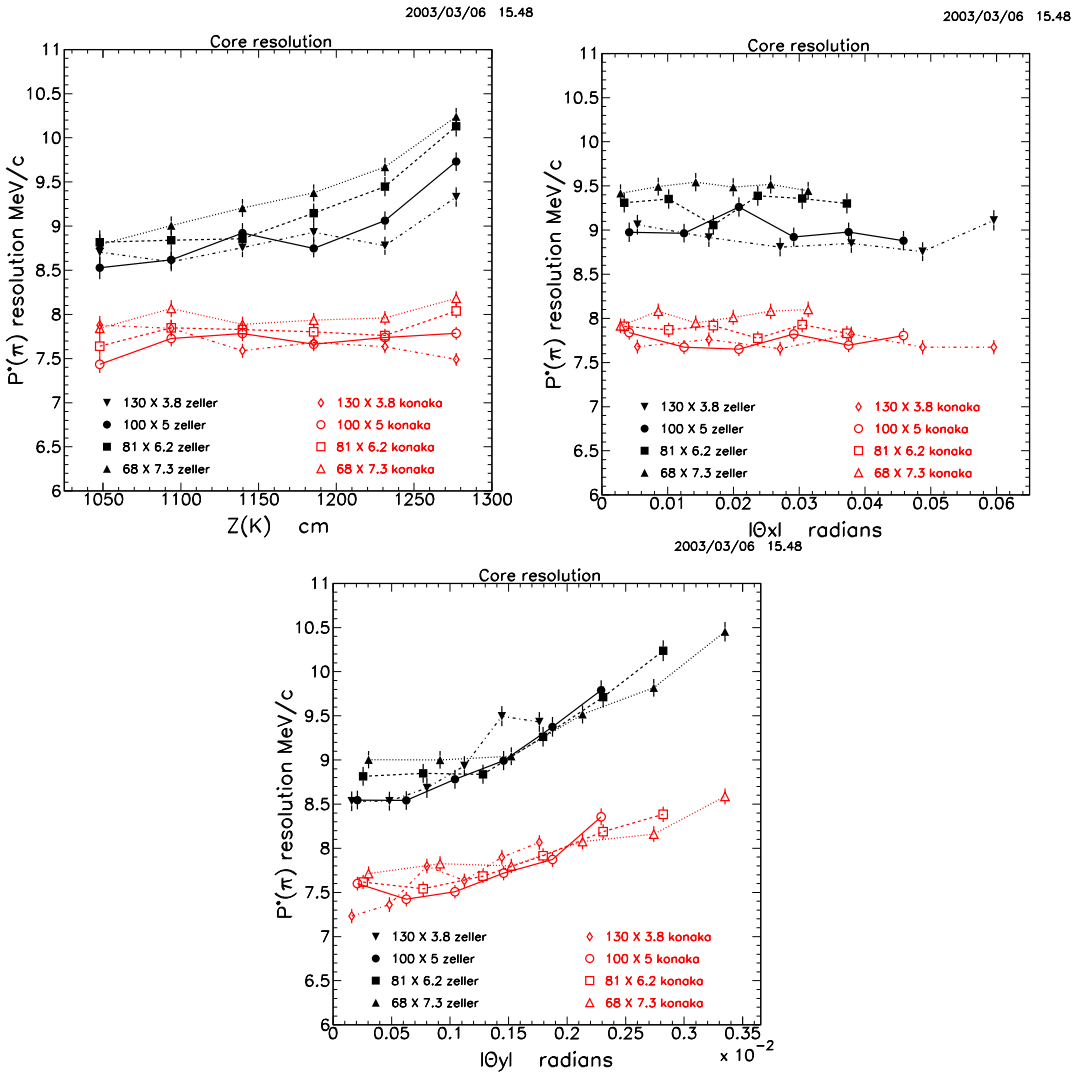

Figure 7: $P^*(\pi^0)$ core resolution as a function of $Z(K)$, $|\Theta_X|$ and $|\Theta_Y|$ for the Konaka and Zeller PR models for the four different beam aspect ratios after application of basic cuts.

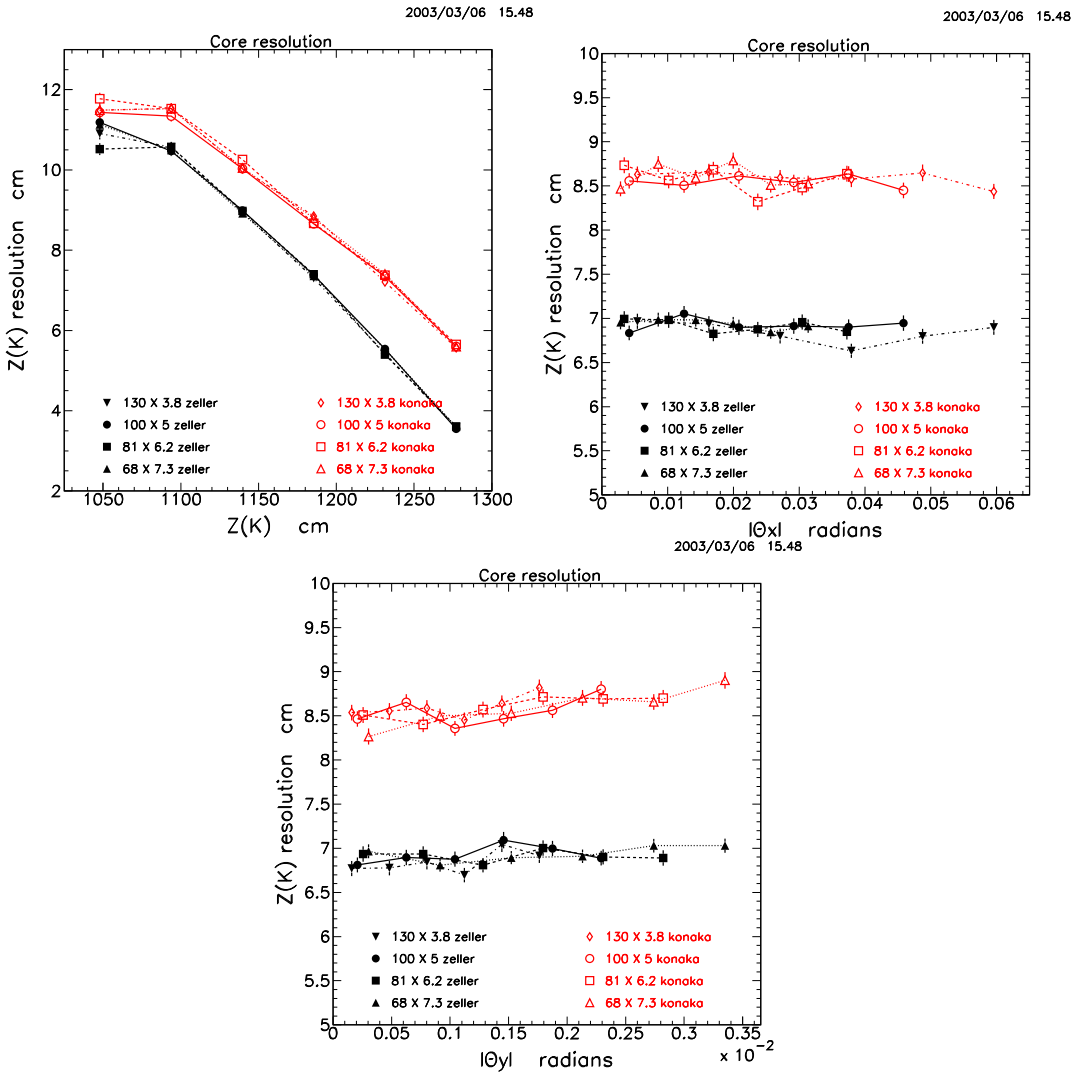

Figure 8: $Z(K)$ core resolution as a function of $Z(K)$, $|\Theta_X|$ and $|\Theta_Y|$ for the Konaka and Zeller PR models for the four different beam aspect ratios after application of basic cuts.

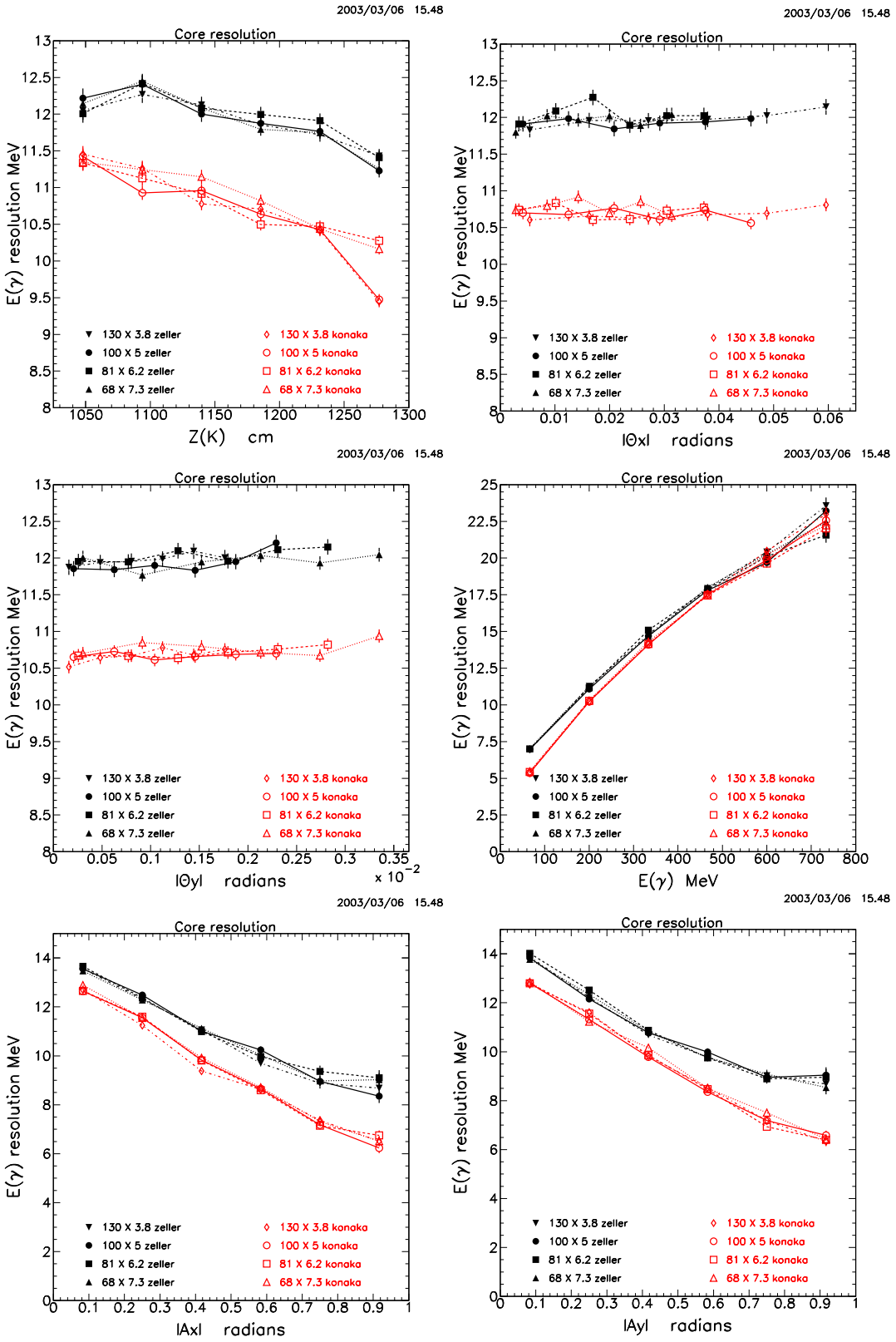

Figure 9: $E(\gamma)$ core resolution as a function of $Z(K)$, $|\Theta_X|$, $|\Theta_Y|$, $E(\gamma)$, $|A_X|$ and $|A_Y|$ for the Konaka and Zeller PR models for the four different beam aspect ratios after application of basic cuts.

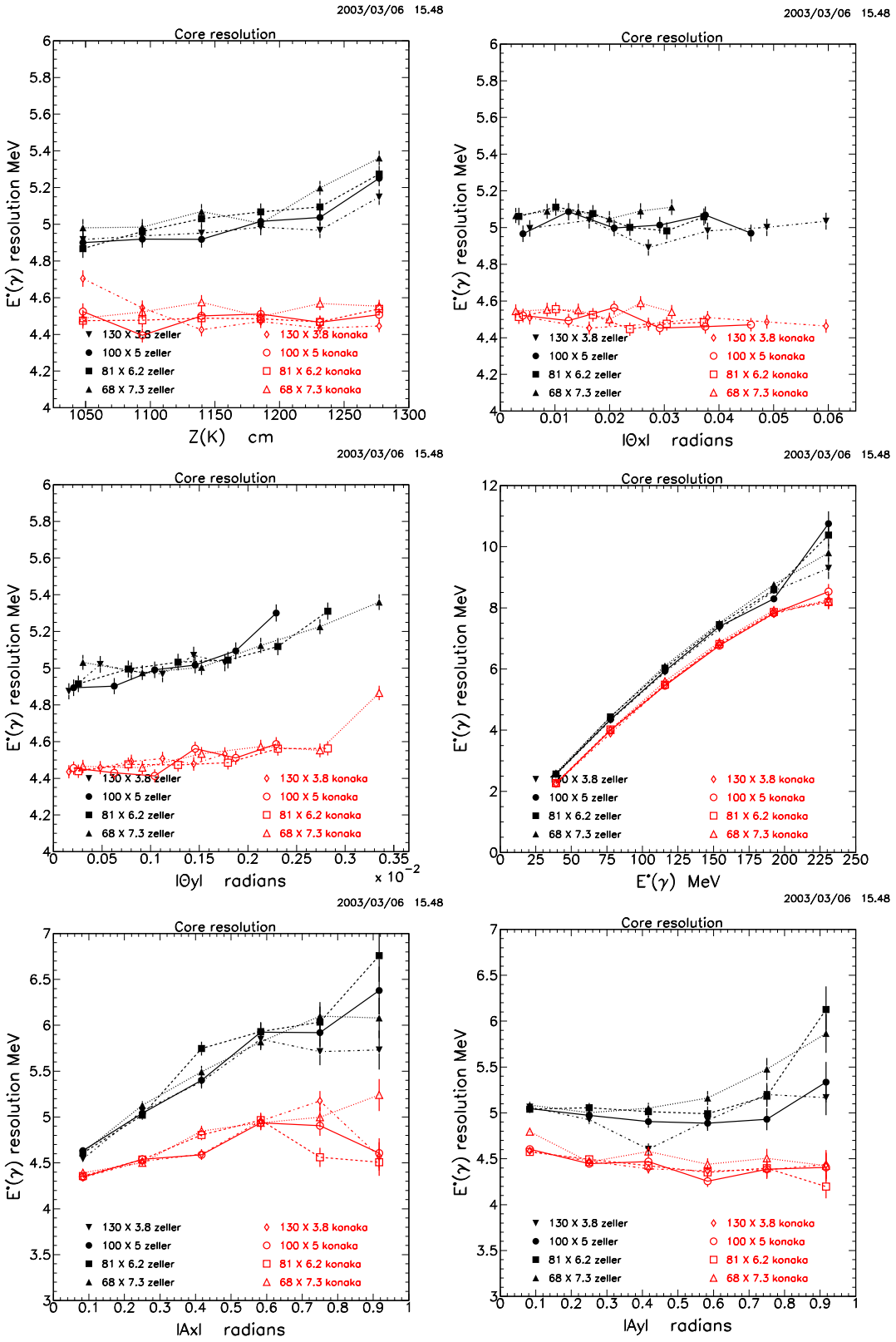

Figure 10: $E^*(\gamma)$ core resolution as a function of $Z(K)$, $|\Theta_X|$, $|\Theta_Y|$, $E^*(\gamma)$, $|A_X|$ and $|A_Y|$ for the Konaka and Zeller PR models for the four different beam aspect ratios after application of basic cuts.

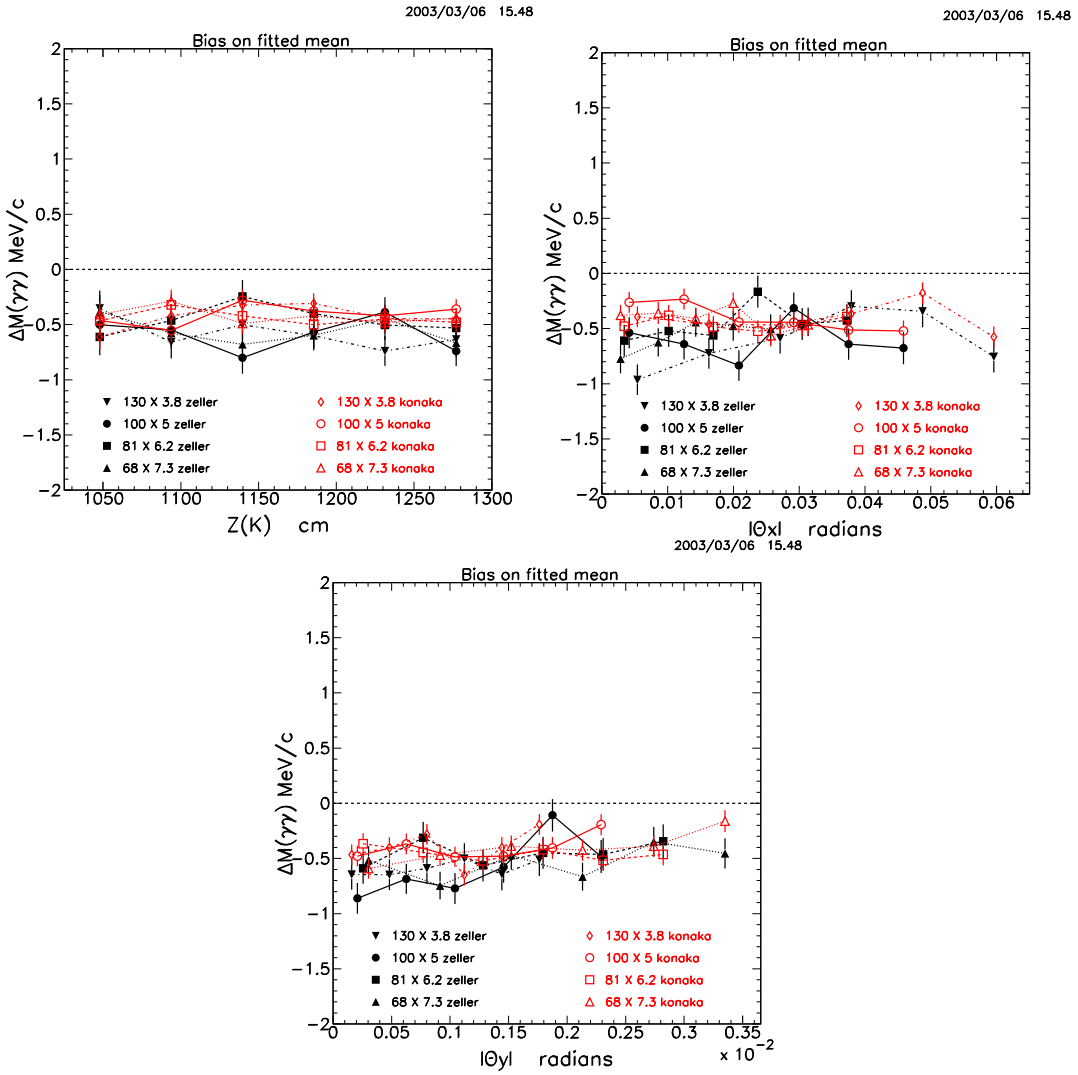

Figure 11: $M(\gamma\gamma)$ bias as a function of $Z(K)$, $|\Theta_X|$ and $|\Theta_Y|$ for the Konaka and Zeller PR models for the four different beam aspect ratios after application of basic cuts.

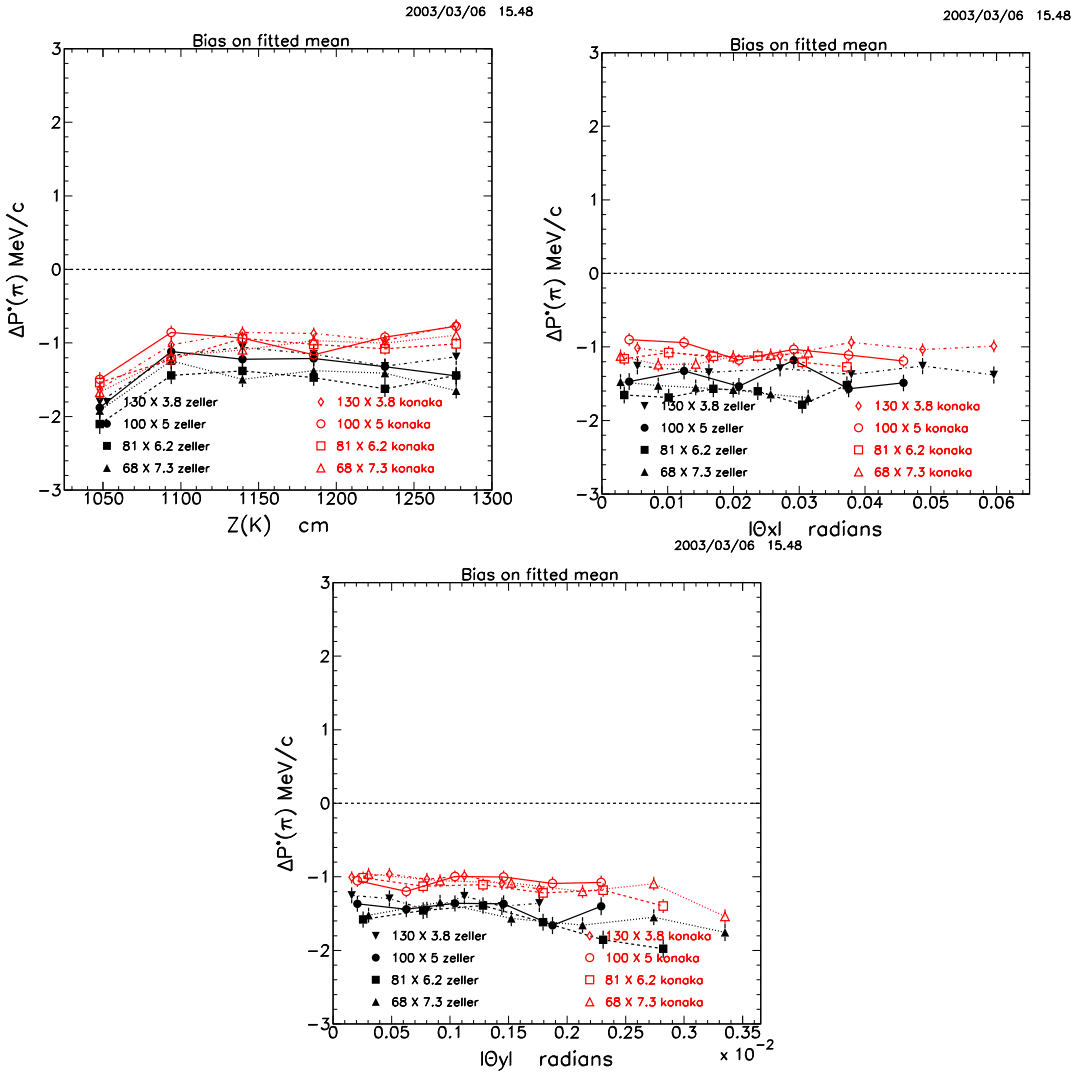

Figure 12: $P^*(\pi^0)$ bias as a function of $Z(K)$, $|\Theta_X|$ and $|\Theta_Y|$ for the Konaka and Zeller PR models for the four different beam aspect ratios after application of basic cuts.

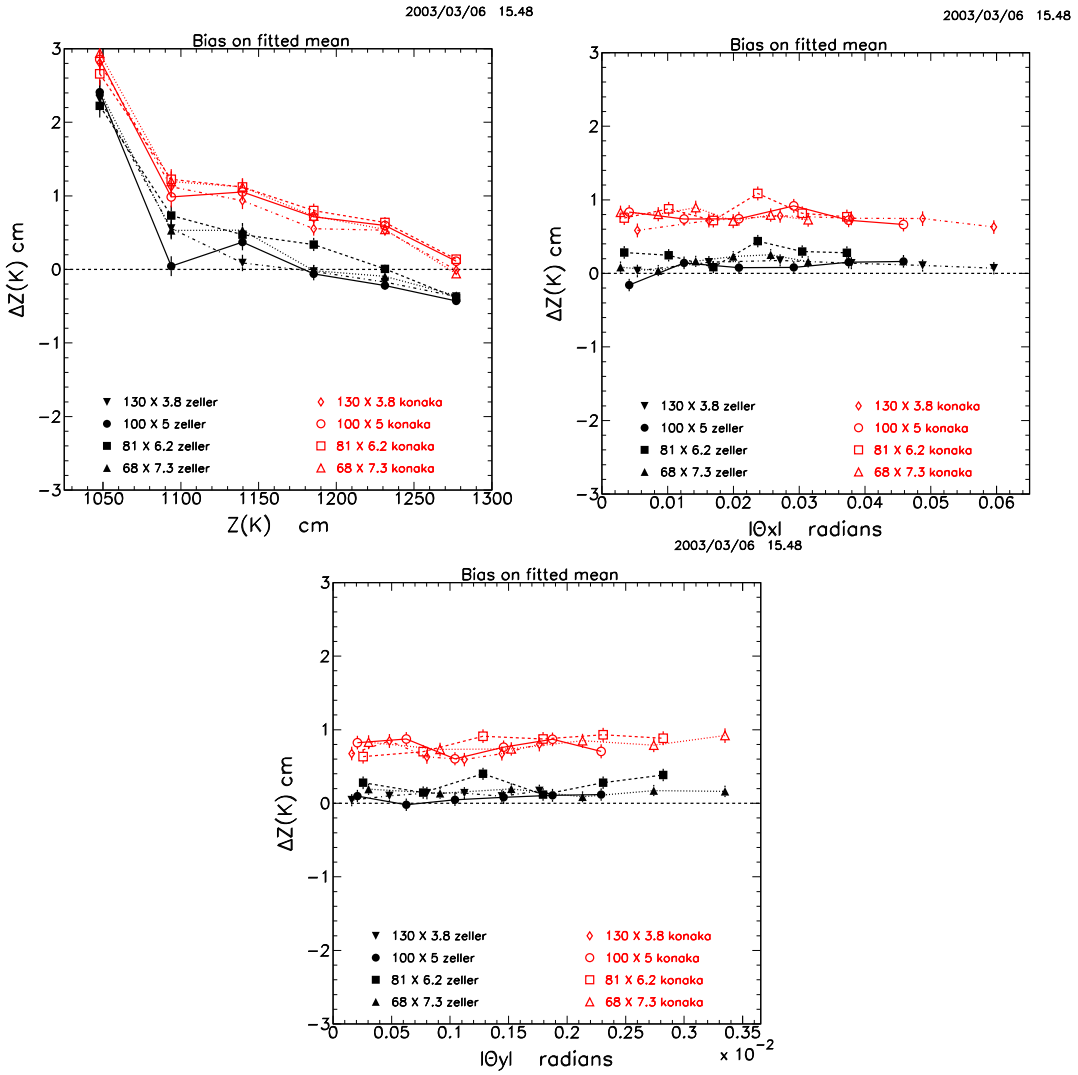

Figure 13: $Z(K)$ bias as a function of $Z(K)$, $|\Theta_X|$ and $|\Theta_Y|$ for the Konaka and Zeller PR models for the four different beam aspect ratios after application of basic cuts.

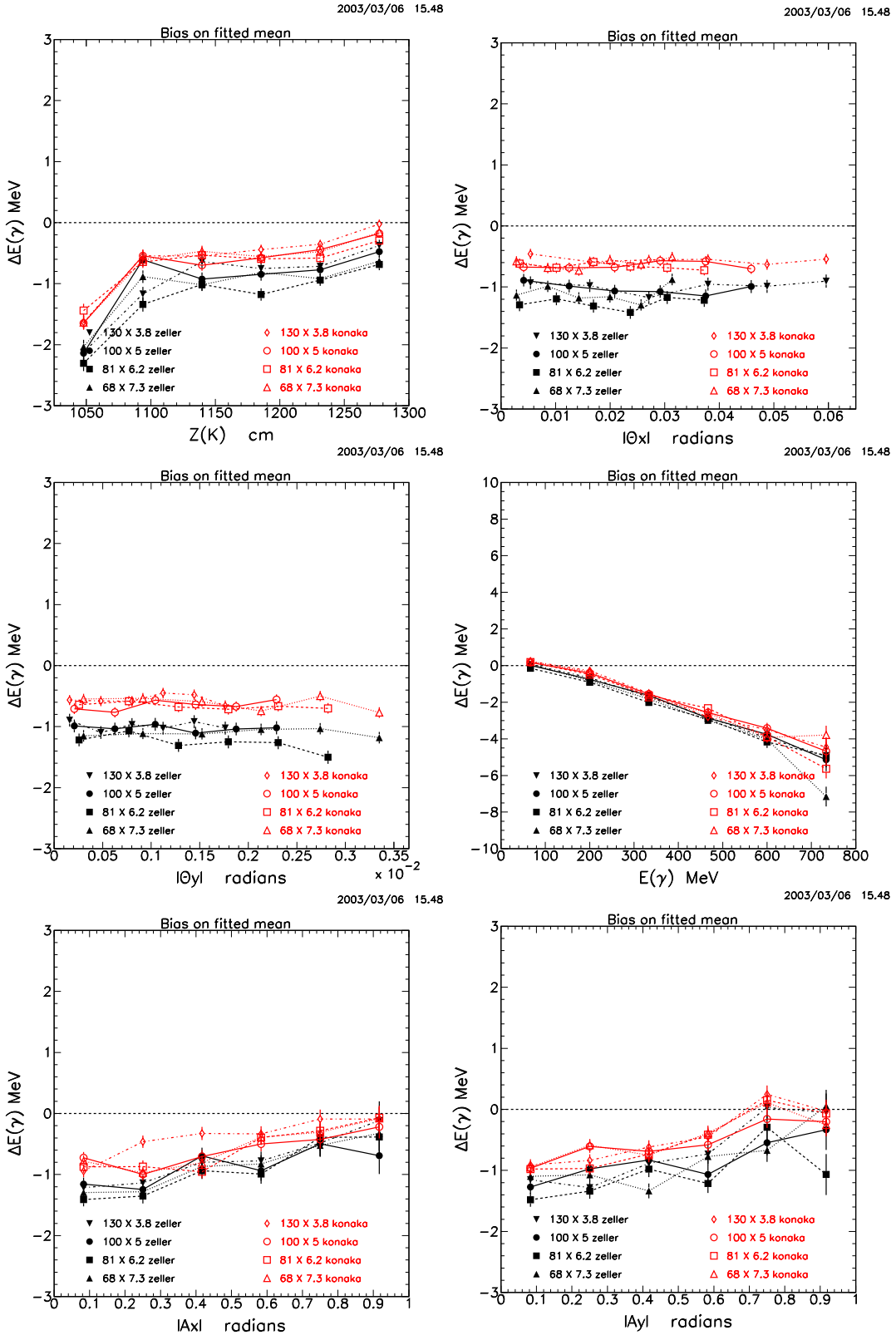

Figure 14: $E(\gamma)$ bias as a function of $Z(K)$, $|\Theta_X|$, $|\Theta_Y|$, $E(\gamma)$, $|A_X|$ and $|A_Y|$ for the Konaka and Zeller PR models for the four different beam aspect ratios after application of basic cuts.

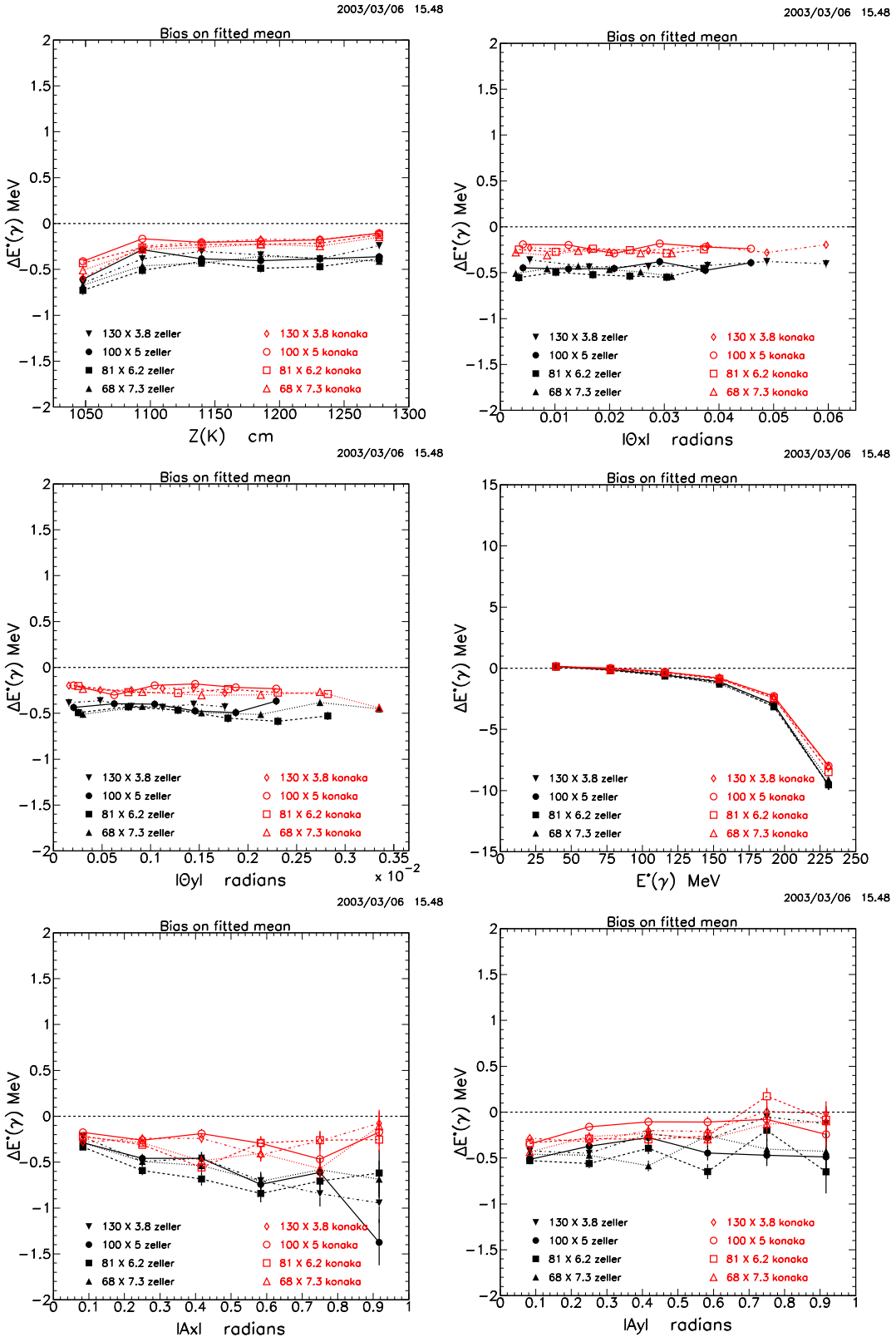

Figure 15: $E^*(\gamma)$ bias as a function of $Z(K)$, $|\Theta_X|$, $|\Theta_Y|$, $E^*(\gamma)$, $|A_X|$ and $|A_Y|$ for the Konaka and Zeller PR models for the four different beam aspect ratios after application of basic cuts.

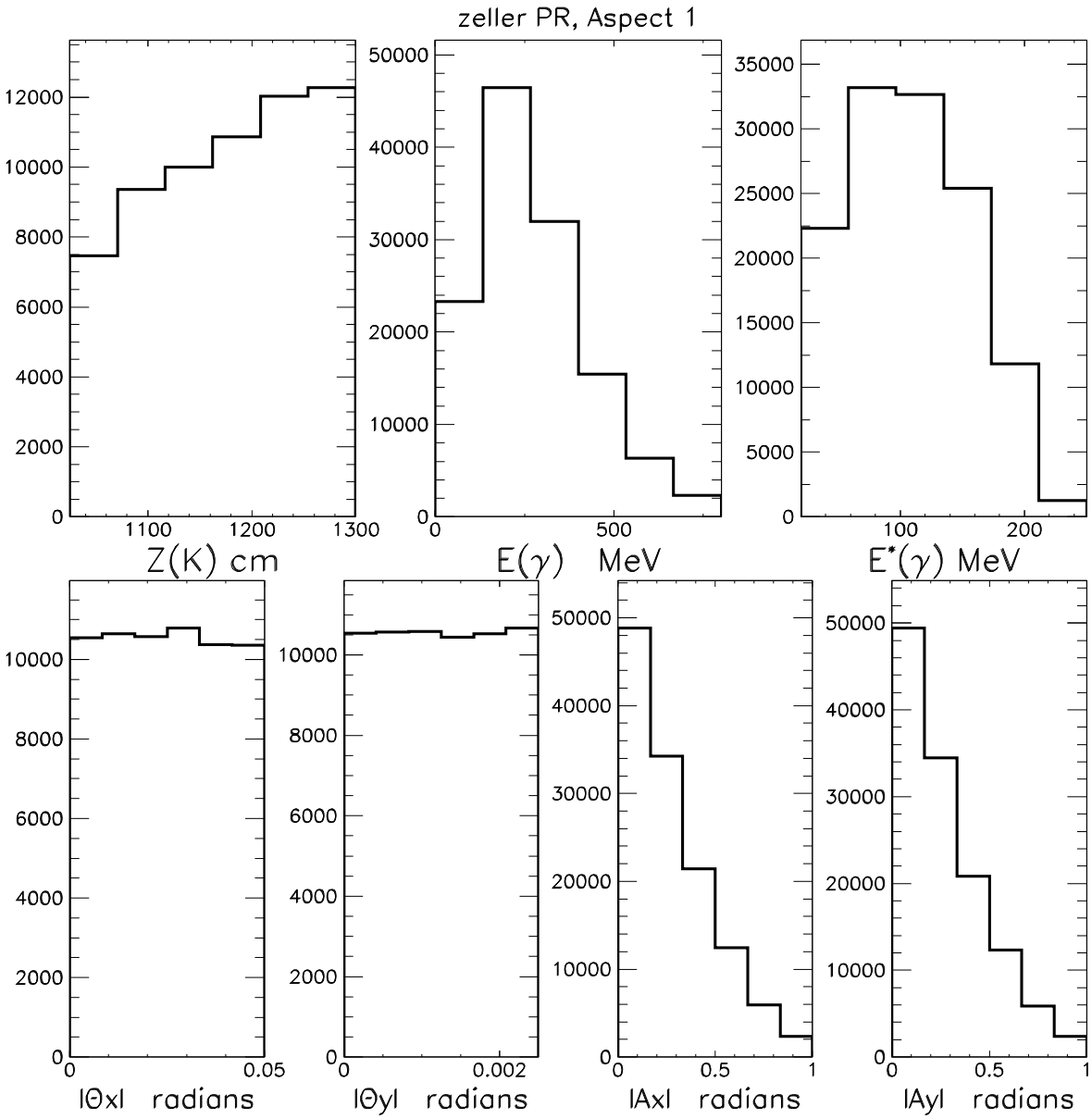

Figure 16: The distributions of $Z(K)$, $E(\gamma)$, $E^*(\gamma)$, $|\Theta_X|$, $|\Theta_Y|$, $|A_X|$ and $|A_Y|$ with the Zeller PR model and the 100×5 mrad^2 aspect ratio after the application of the **basic cuts**.

5 Acceptance

Figures 17 and 18 show S/B *vs* signal for the four different beam aspect ratios. The calculated signal rate with the Zeller PR model is significantly less than of that with the Konaka PR model as described in Section 3. At the $\sim 10\%$ level of statistical precision, there is no significant difference in the S/B *vs* signal curves for the four different aspect ratios with the Konaka PR model as seen in Figure 18. However, there is a significant loss of acceptance between the two narrower and taller aspect ratios and the wider and shorter aspect ratios with the Zeller PR model as seen in Figure 17. The size of the FastMC samples with the Zeller PR model are three to four times larger than that for the Konaka PR model.

The ratio of S/B for the 81×6.1 mrad^2, 68×7.3 mrad^2 and 130×3.8 mrad^2 configurations to the S/B for the 100×5 mrad^2 configuration as a function of the expected signal yield with the Zeller PR model is shown in Figure 19. The value of S/B and its uncertainty for each configuration at each value of signal yield was estimated from the results shown in Figures 17 and 18 by interpolation. The central plot in Figure 19 clearly shows a drop in S/B of $20 \pm 5\%$ or more for signal yields of 50 events or more. There is a drop in S/B for yields of less than 50 events although with less statistical precision ($18 \pm 8\%$ at 36 signal events, $17 \pm 9\%$ at 25 signal events). The degradation in the $M(\gamma\gamma)$, $P^*(\pi^0)$ and $E^*(\gamma)$ resolution with larger K^0_L vertical production angles is the most likely explanation of the drop in acceptance.

A similar comparison with the Konaka PR model in Figure 20 confirms the consistency of the yields for the different aspect ratios.

The signal, background and signal/background as a function of the vertical beam divergence with the Zeller and Konaka PR models are shown in Figures 21 and 22, respectively. The signal yield reduction with increasing vertical beam divergence is linear to a good approximation for both PR models. The background reduction is also roughly linear but with a more shallow slope. From the quadratic fit to the four vertical beam divergence points, the maximum signal/background appears to be with a vertical beam divergence of 5 to 6 mrad for the Zeller PR model.

The $2\pi^0$, $3\pi^0$ and $\pi e\nu\gamma$ background rates as a function of the vertical beam divergence with the Zeller and Konaka PR models are shown in Figures 23 and 24, respectively. With the Zeller PR model, the $\pi e\nu\gamma$ background decreases and the $3\pi^0$ background increases with increasing vertical beam divergence. The behavior of the $2\pi^0$ background as a function of the vertical beam divergence is a function of the cut severity. The $2\pi^0$ background decreases as the vertical beam divergence increases for the looser cuts and is constant or increases slightly with the tighter cuts.

Due to this degradation of resolution, adjusting the cuts for the 81×6.1 mrad^2 or 68×7.3 mrad^2 configurations is unlikely to produce a better S/B without a loss of signal yield.

6 Conclusions and additional questions

Narrower and taller beam aspect ratios with respect to the 100×5 mrad^2 configuration used in the TDR have significantly lower acceptance with the Zeller PR model due to the degradation in $M(\gamma\gamma)$, $P^*(\pi^0)$ and $E^*(\gamma)$ resolution. The degradation in resolution for these quantities is less severe with the Konaka PR model and no significant difference in acceptance is seen between aspect ratios ranging from 68×7.3 mrad^2 to 130×3.8 mrad^2.

Questions to be addressed in subsequent note(s):

1. How realistic are the PR models? The Konaka PR model neglects possible angular dependence of the angular resolution. The Zeller PR model assumes only cathode strip readout and neglects possible amelioration with anode readout of the angular resolution at large angles.

2. The $20 \pm 5\%$ ($18 \pm 5\%$) reduction in signal for the 68×7.3 mrad^2 (81×6.1 mrad^2) configuration appears to be larger than one would expect from the degradation in core resolution between the Konaka and Zeller PR models. Can the cuts be adjusted to produce better S/B for larger vertical beam divergence than 5 mrad?

3. How important is the production angle dependence of the K_L^0 and neutron flux?

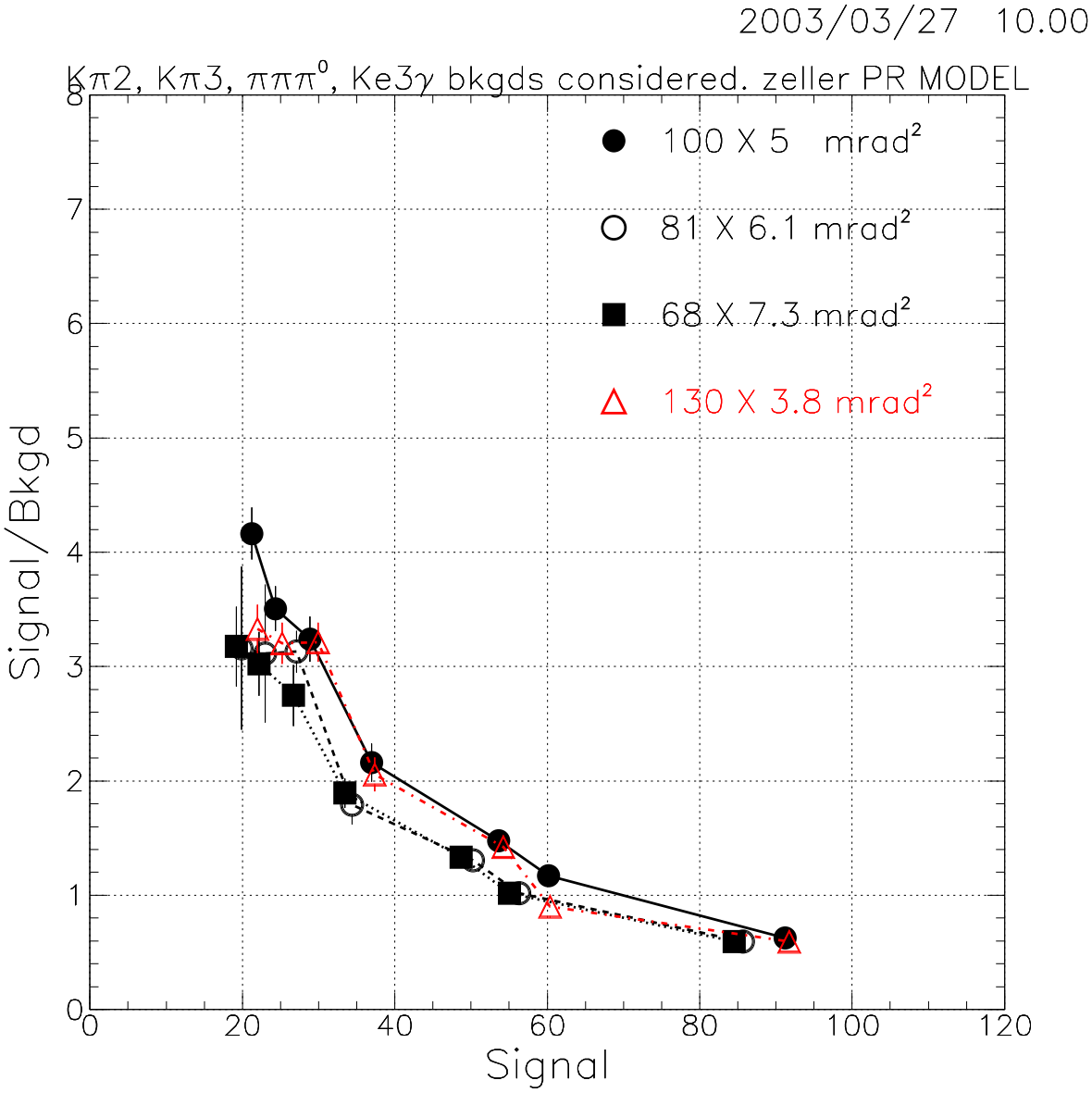

Figure 17: Signal/Background *vs* signal for the four different beam aspect ratios shown with the Zeller PR model. The uncertainties are statistical only and are correlated from point to point.

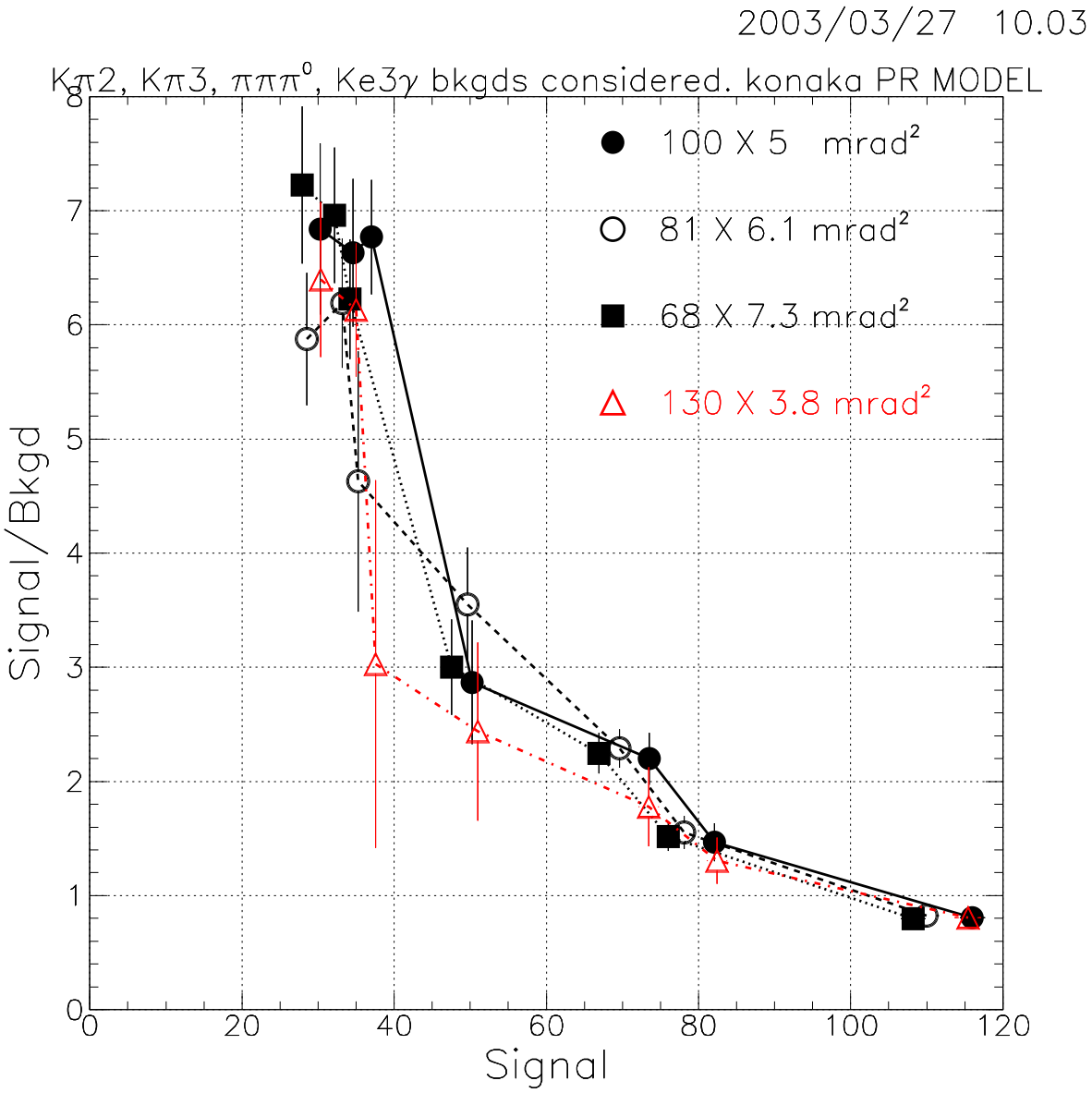

Figure 18: Signal/Background *vs* signal for the four different beam aspect ratios shown with the Konaka PR model. The uncertainties are statistical only and are correlated from point to point.

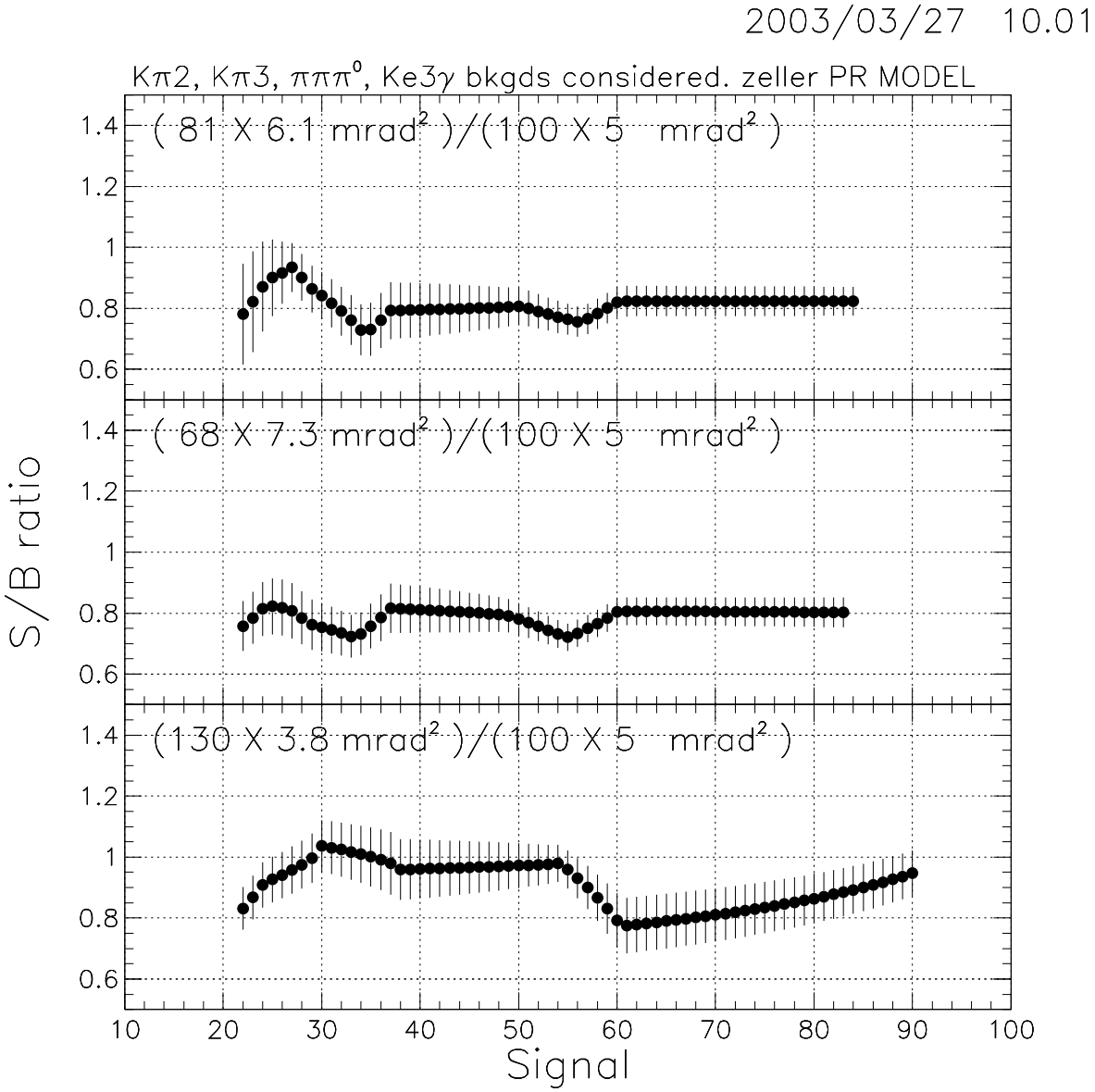

Figure 19: Signal/Background for the three different beam aspect ratios compared to the 100×5 mrad^2 aspect ratio with the Zeller PR model. The uncertainties are statistical only and are correlated from point to point. See text for details.

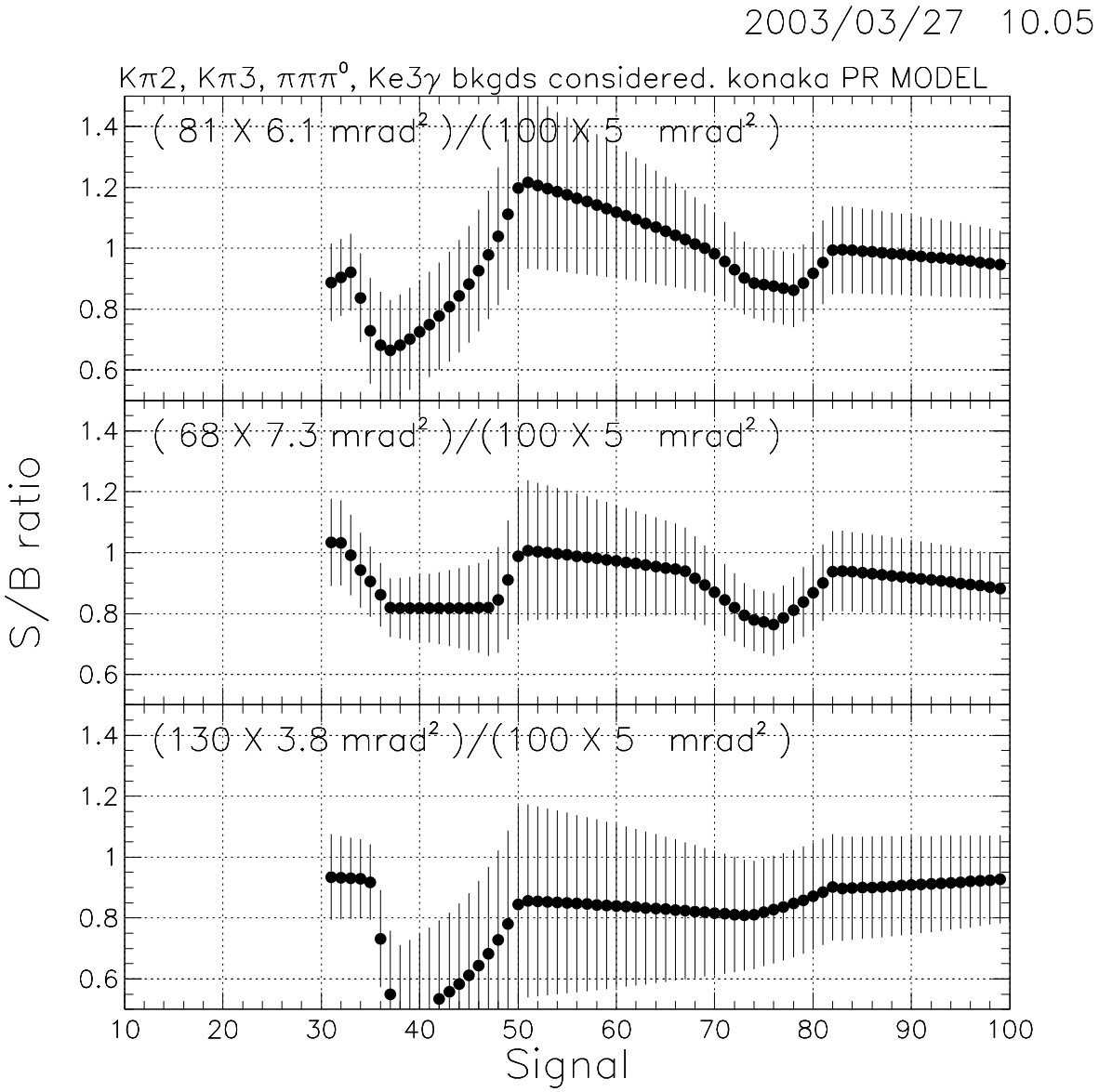

Figure 20: Signal/Background for the three different beam aspect ratios compared to the 100×5 mrad^2 aspect ratio with the Konaka PR model. The uncertainties are statistical only and are correlated from point to point. See text for details.

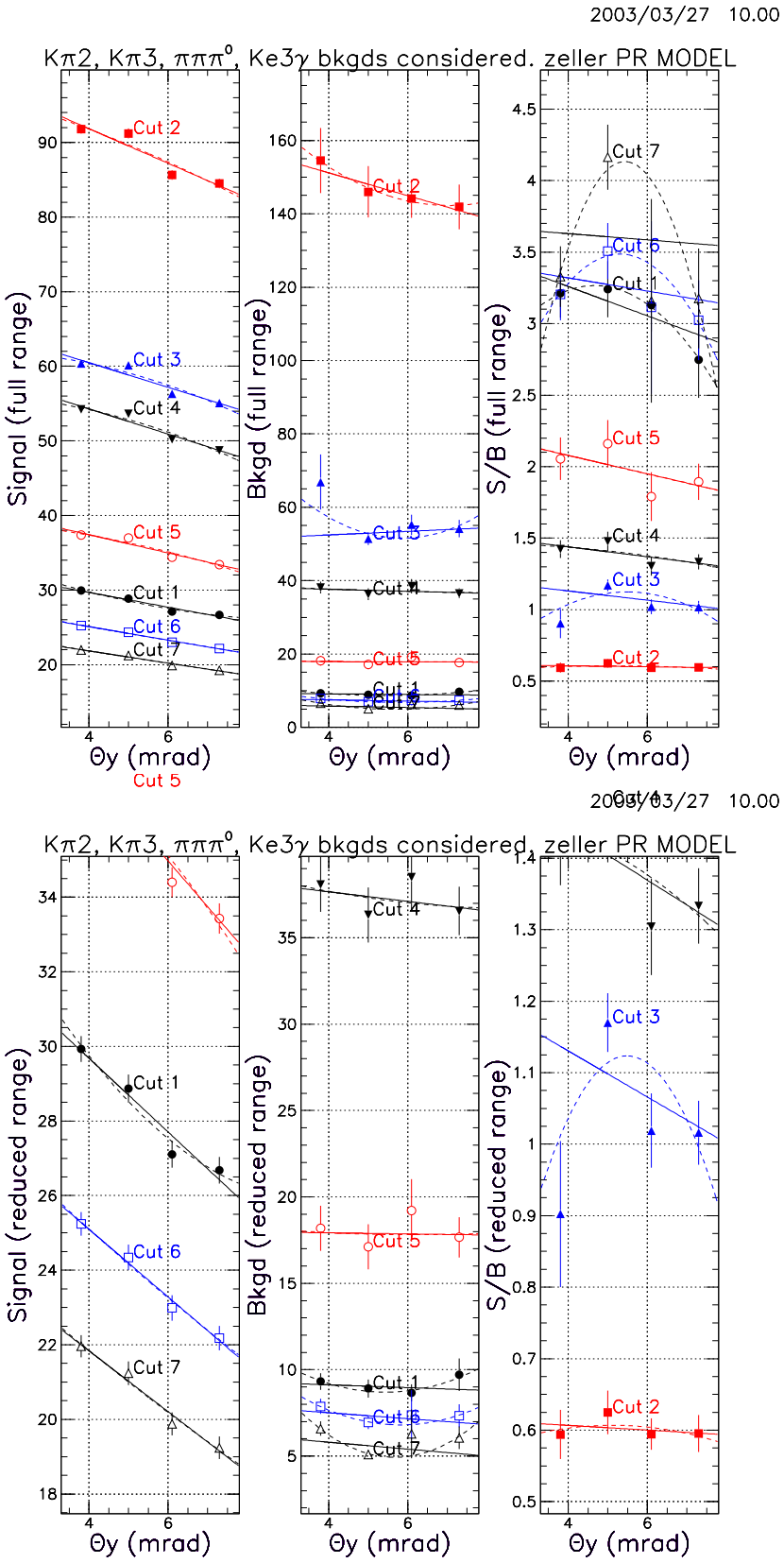

Figure 21: The signal, background and signal/background as a function of the vertical beam divergence with the Zeller PR model for each of the seven sets of cuts. The results of linear and quadratic fits are shown as solid and dashed lines, respectively.

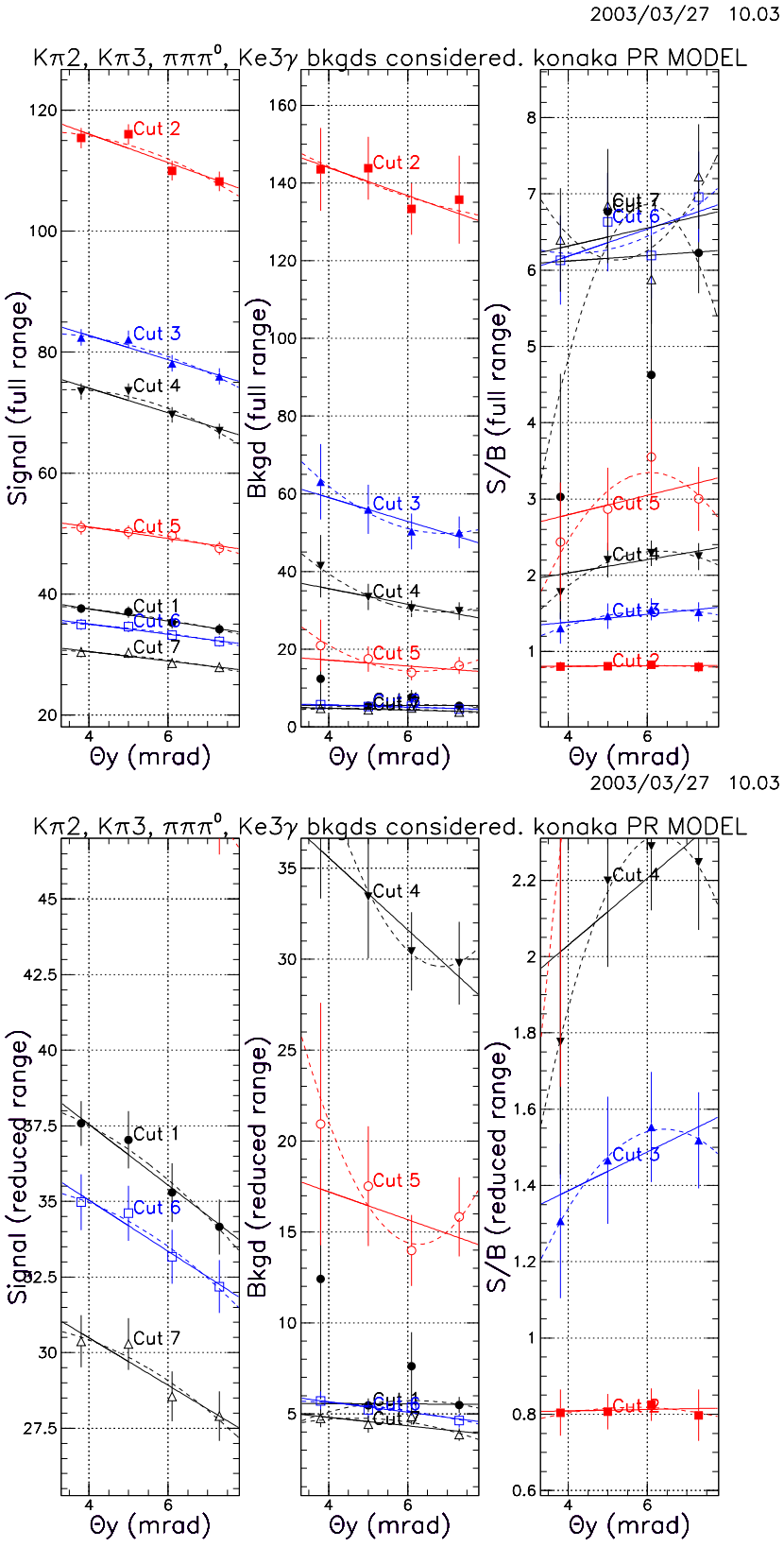

Figure 22: The signal, background and signal/background as a function of the vertical beam divergence with the Konaka PR model for each of the seven sets of cuts. The results of linear and quadratic fits are shown as solid and dashed lines, respectively.

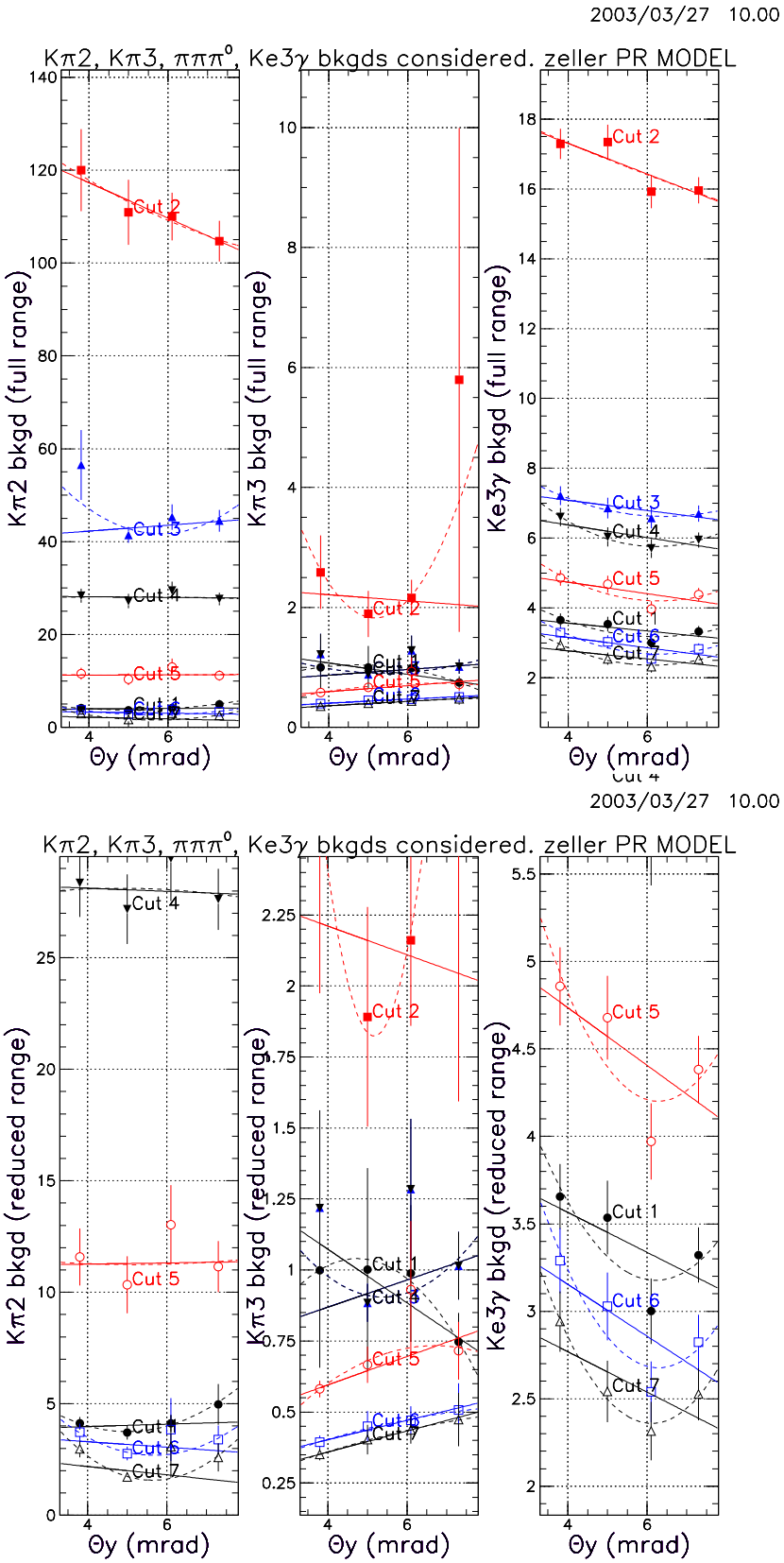

Figure 23: The $2\pi^0$, $3\pi^0$ and $\pi e\nu\gamma$ background rates as a function of the vertical beam divergence with the Zeller PR model for each of the seven sets of cuts. The results of linear and quadratic fits are shown as solid and dashed lines, respectively.

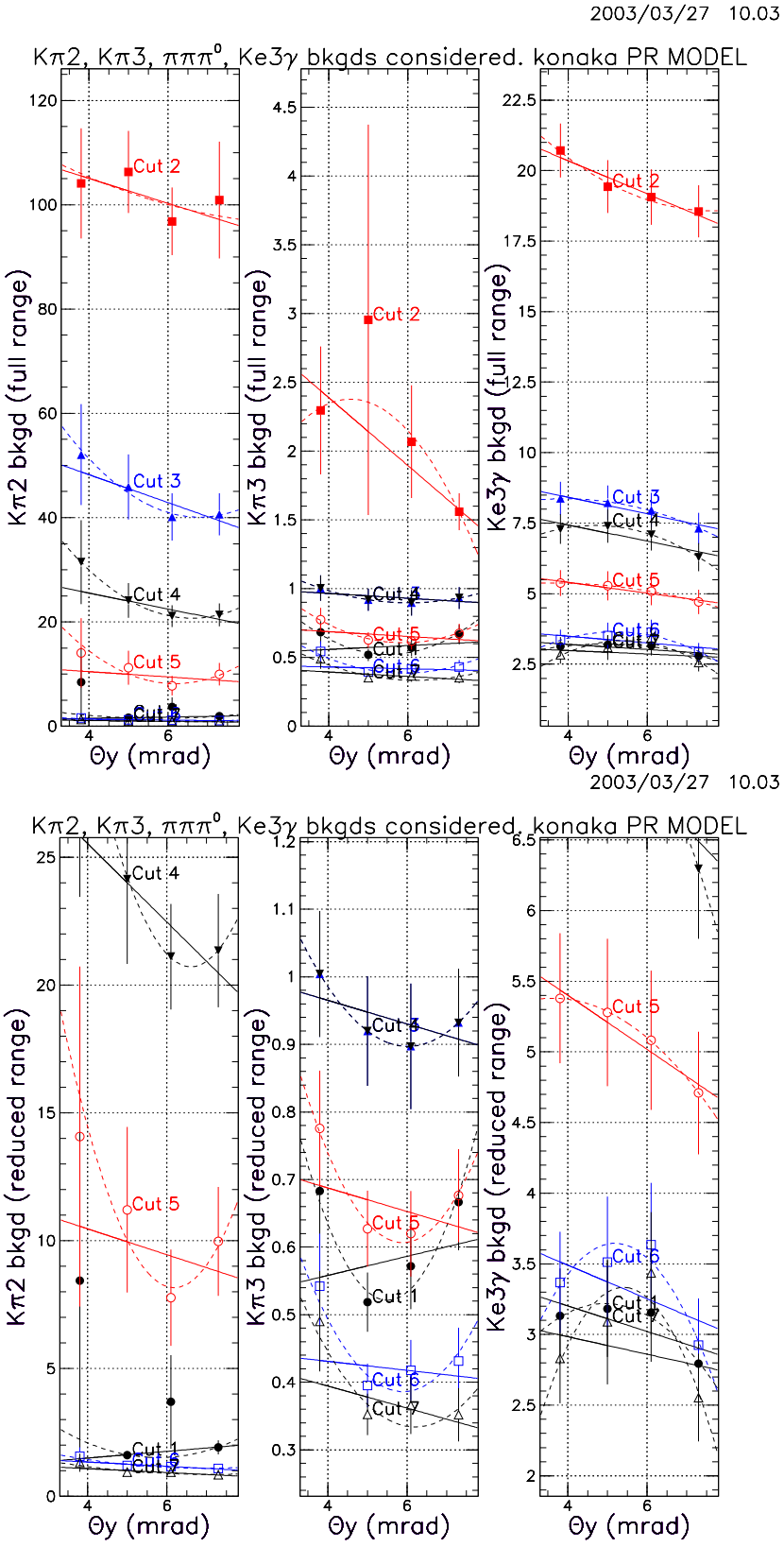

Figure 24: The $2\pi^0$, $3\pi^0$ and $\pi e\nu\gamma$ background rates as a function of the vertical beam divergence with the Konaka PR model for each of the seven sets of cuts. The results of linear and quadratic fits are shown as solid and dashed lines, respectively.

References

[1] "KOPIO: Measurement of the decay $K_L \to \pi^\circ \nu\bar{\nu}$, Draft Technical Design Report for the National Science Foundation, TDR, 8 June 2001.

[2] J. Doornbos, "Comparison of the neutron halos for 4 different x-y aspect ratios, for momenta above 750 MeV/c", KOPIO Technical Note TN049, 14 Feb 2003.

[3] D.E. Jaffe, "FastMC estimate of neutron background rates", KOPIO Technical Note TN047, 16 Dec 2002.

[4] P. Kapinos " The estimation of Klong flux at 24 Gev/c", KOPIO Technical Note TN005, 22 Aug 1997.

[5] D. Bryman, "E926 Preradiator Study: Alternating Horizontal and Vertical Anode Wires and Cathode Strips" , KOPIO Technical Note TN014, 25 March 1999.

[6] M. Zeller, "A preradiator for E926 based on a Straw Tube design", KOPIO Technical Note TN006, 2 March 1998.

List of Tables

List of Figures